

**KU LEUVEN**

 **FACULTEIT  
INGENIEURSWETENSCHAPPEN**

# Next generation brain implant for distributed recordings of cellular activity in freely behaving rodents

Rik van Daal

Thesis submitted for the degree of  
Master of Science in  
Biomedical Engineering

**Thesis supervisors:**

Prof. Robert Puers  
Prof. Fabian Kloosterman

Academic year 2017 – 2018

**Master of Science in Biomedical Engineering**

# Next generation brain implant for distributed recordings of cellular activity in freely behaving rodents

Rik van Daal

Thesis submitted for the degree of  
Master of Science in  
Biomedical Engineering

**Thesis supervisors:**

Prof. Robert Puers  
Prof. Fabian Kloosterman

**Assessors:**

Prof. Alexander Bertrand  
Prof. Wim Dehaene  
Dr. Frederik Ceysens

**Mentor:**

Dr. Jyh-Jang Sun

© Copyright KU Leuven

Without written permission of the thesis supervisors and the author it is forbidden to reproduce or adapt in any form or by any means any part of this publication. Requests for obtaining the right to reproduce or utilize parts of this publication should be addressed to Faculteit Ingenieurswetenschappen, Kasteelpark Arenberg 1 bus 2200, B-3001 Heverlee, +32-16-321350.

A written permission of the thesis supervisors is also required to use the methods, products, schematics and programs described in this work for industrial or commercial use, and for submitting this publication in scientific contests.

## Preface

I started my master's thesis at 3 September 2018 within two academic research groups: '*Neuro-Electronics Research Flanders (NERF)*' which is located within '*Interuniversitair Micro-Electronica Centrum (IMEC)*' and '*Micro-elektronica en Sensoren (MICAS)*' which is a division of the department of electrical engineering (ESAT) of '*Katholieke Universiteit Leuven (KU Leuven)*'.

The long-term goal of NERF is the thorough understanding of brain functioning and development of novel medical applications to diagnose and treat neurological disorders. Sophisticated tools and electronic technologies are required to advance this understanding.

MICAS possesses a cleanroom within Leuven NanoCentre and realizes breakthroughs in the micro- and nano-electronics sector. The co-operation through MICAS and NERF is the excellent combination for advancing neurological research. New flexible polyimide probes were micromachined in the cleanroom and a novel implantation system was 3D-printed at NERF. The entire system was validated *in-vivo* within NERF.

## Acknowledgements

It was a great pleasure to be part of both research groups. The people within both groups inspired, motivated and helped me doing this fascinating research about the next generation brain implant. For the development of the flexible probes I would like to thank Dr. Frederik Ceysens. Without his knowledge, knowhow and business relations the result would not have been accomplished. I like to thank Thomas Brockhans for helping me to laser cut the stainless steel shuttles. For the production of the titanium 3D-printed exit tip I would like to thank Louca Goossens from the additive manufacturing group of KU Leuven. I also want to thank my student colleague Tomas Fiers for helping me to process the electrophysiological signals. I'm very grateful to my supervisors prof. Fabian Kloosterman and prof. Bob Puers to enable this research and supporting me during the entire thesis period. My special thanks goes to my mentor Dr. Jyh-Jang Sun for his great support, coaching and feedback to improve my master's thesis. After all I would like to thank my student colleagues, family and Julie for their great support during my entire study at KU Leuven.

## Table of contents

Preface.....	i
Acknowledgements.....	i
Summary .....	iv
List of figures .....	v
List of tables .....	vi
List of abbreviations .....	vi
Chapter 1: General introduction .....	1
1.1 Brain implant for advancing the knowledge about memory functioning.....	3
1.2 Thesis objective .....	4
Chapter 2: Flexible polyimide probes.....	6
2.1 State-of-the-art.....	6
2.2 Design phase.....	8
2.3 Method.....	11
2.4 Materials and determination of process parameters .....	12
2.5 Fabrication process .....	15
2.5.1 Wafer and cleaning.....	16
2.5.2 Evaporation of the sacrificial layer .....	16
2.5.3 Polyimide deposition.....	17
2.5.4 Photolithography and mask development.....	18
2.5.5 Metal deposition and lift-off .....	20
2.5.6 Top polyimide deposition and patterning.....	20
2.6 Results .....	22
2.7 Discussion .....	23
Chapter 3: Hyperdrive, the probe positioning mechanism.....	25
3.1 State-of-the-art.....	25
3.2 Design phase.....	28
3.2.1 Microdrives: screw-driven shuttles.....	29
3.2.2 Polyimide tubes and exit tip .....	31
3.2.3 Skull attachment structure .....	32
3.2.4 Electronic interface board with zero-insertion-force connectors.....	32
3.2.5 External shell and protective caps.....	33
3.3 Fabrication processes .....	34
3.3.1 3D-printed parts .....	34
3.3.2 Laser-cut stainless steel shuttles.....	35
3.3.3 Direct metal laser sintering of the exit tip.....	38

3.4 Assembly of the hyperdrive.....	39
3.5 Results .....	40
3.6 Discussion .....	41
Chapter 4: Validation of the brain implant .....	44
4.1 Insertion test .....	44
4.2 Electrical test .....	45
4.3 In-vivo test.....	46
4.3.1 Surgical procedure.....	46
4.3.2 Recorded data .....	48
4.4 Discussion .....	50
Chapter 5: Discussion .....	51
References.....	53
Annexes .....	57
A: Method of the literature study .....	57
B: Results and methods for the individual wafers .....	59
C: Individual part weights of the hyperdrive.....	63
D: Channel mapping .....	64
E: Probe configuration within the hyperdrive .....	64
F: Impedance values of probes within hyperdrive .....	65

## Summary

In the twenty-first century neurological disorders are still impacting the lives of a large number of individuals. The outcomes of neuroscience in mind and brain functioning will tremendously influence the healthcare sector by evolving the treatments for various disorders and advancing the development of sophisticated tools. Brain functioning involves various cognitive processes for accomplishing simple to very complex tasks, this is where distributed brain regions are interacting. The power of the brain comes from the enormous amount, diversity, and interactions between the neurons. One of the great neuro-technological challenges is to record the activity of thousands of neurons simultaneously to acquire more knowledge about the interaction of distributed brain regions.

Long-term invasive electrophysiological recordings of neural activity in freely behaving animals are indispensable to understand how the brain performs computations and supports cognition.

The goal of this thesis was the development of a: 'next generation brain implant for distributed recordings of cellular activity in freely behaving rodents'.

The novel brain implant contains 16 individually lowerable flexible polyimide probes with 16 recording electrodes each, adding up to a total of 256 recording sites. The probes are micromachined and the brain implant is 3D-printed by stereolithography. Each probe is lowered by a screw-driven shuttle and guided through a 3D-printed titanium exit tip before penetrating the rat's brain. The total travel distance is 8 mm. Compared to the previous brain implant used at NERF: 1) the dimensions and weight are significantly less, 2) the assembly time is drastically reduced, and 3) the electronic components are well protected against extended experimental handling.

Three validation tests were performed: 1) an insertion test revealed that the probes fully penetrated a brain simulation gel, but bended off track after three-fourths insertion. 2) The electrical impedance test showed that the initially impedance values were too high ( $>1\text{M}\Omega$ ) for performing electrophysiological experiments. It required a gold plating step to lower the impedance values to a mean value of  $331\text{k}\Omega$  with a sample standard deviation of  $71\text{k}\Omega$ , excluding the outliers. 3) The brain implant was tested *in-vivo* and electrophysiological recordings were obtained. This is the most considerable proof for the novel brain implant.

In the future more advanced techniques, like motors, wireless connectors or signal processing chips can be implemented into the brain implant. Those techniques will improve the electrophysiological recordings and enable complex behavioural experiments which are necessary to advance the understanding of brain functioning. This knowledge will evolve the treatments for various neurological diseases and will tremendously impact the entire healthcare sector. Nevertheless, this can only be realized by implementing sophisticated tools like the brain implant presented in this thesis.

## List of figures

Figure 1: Freely behaving rat carrying a brain implant on its skull .....	2
Figure 2: 3D model and slice of a rat's brain .....	3
Figure 3: Cross-section of the conceptual drawing of the next generation brain implant .....	4
Figure 4: Overview of the various electrode wire inventions. ....	7
Figure 5: Probes showing patterned electrode configurations.....	8
Figure 6: Designed probe configurations. ....	10
Figure 7: Virtual pattern on a 4" wafer with the different probe designs .....	11
Figure 8: Illustration of resist development problems.....	12
Figure 9: Possible problems that can occur with lift-off .....	13
Figure 10: Debris particles between the electrode lines.....	13
Figure 11: The deposited metal connector pads are loosened by the ultrasonic bath .....	13
Figure 12: Measuring probes on two adjacent connector pads to determine cross-talk .....	14
Figure 13: Fabrication sequence of the polyimide probes .....	15
Figure 14: Silicon wafer with water droplets .....	16
Figure 15: Balzers Med 010 evaporation tool .....	17
Figure 16: Pre-baking temperature profile for polyimide .....	18
Figure 17: Laser mask writer .....	18
Figure 18: Lift-off resist profile.....	19
Figure 19: Post-baking temperature profile for polyimide .....	21
Figure 20: Measuring the probe profile with a profilometer to determine the layer thicknesses .....	22
Figure 21: Flexible polyimide probe with a 2x8 electrode configuration .....	22
Figure 22: Line failures resulting in disconnected channels.....	23
Figure 23: Hyperdrive by Kloosterman et al.....	25
Figure 24: Hyperdrive chronology.....	28
Figure 25: Four types of microdrives .....	29
Figure 26: Custom made microdrive screw adapted from Kloosterman et al. ....	30
Figure 27: Custom designed shuttles .....	30
Figure 28: Two exit tip designs.....	31
Figure 29: Electronic Interface Board (EIB) and Headstage. ....	32
Figure 30: Formlabs Form 2 3D-printer.....	34
Figure 31: Inside Formlabs Form 2 3D-printer .....	34
Figure 32: Basic principle of a laser cutter .....	36
Figure 33: Drawing of the cutting pattern for 10 microdrive shuttles.....	37
Figure 34: Prototype of the final holder.....	37

Figure 35: Final version of the hyperdrive .....	40
Figure 36: Proposed exit tip design for easier insertion of polyimide tubes .....	41
Figure 37: Proposal for a dual exit tip for targeting at least two different brain areas .....	41
Figure 38: Proposed EIB designs .....	42
Figure 39: Flexible polyimide probe lowered in 0.6% agarose gel for insertion validation .....	44
Figure 40: Mean impedance values before and after gold plating for the 2x8 probe. ....	46
Figure 41: Freely behaving animal one day after the implantation .....	47
Figure 42: Hippocampal sharp-wave-ripples recorded by a 2x8 probe .....	48
Figure 43: Zoomed section of the sharp-wave-ripple of channel 16 .....	48
Figure 44: Eight isolated units recorded by a 2x8 probe.....	49
Figure 45: Filtering procedure for the literature study. ....	58

## List of tables

Table 1: Design requirements and specifications of the flexible probes .....	8
Table 2: Features of the produced flexible polyimide probes .....	23
Table 3: Gold plating sequence .....	45
Table 4: Impedance values of the electrodes of a 2x8 probe .....	45

## List of abbreviations

CAD	Computer-Aided-Design
CA1	Cornu Ammonis 1
CNC	Computer numerical control
DMLS	Direct Metal Laser Sintering
EIB	Electronic Interface Board
HCl	Hydrochloric acid
HF	Hydrofluoric acid
HNO <sub>3</sub>	Nitric acid
LASER	Light amplification of stimulated emission of radiation
LOR	Lift-off resist
NERF	Neuro-Electronics Research Flanders
NMP	N-Methyl-2-pyrrolidone
SLA	Stereolithography
S1818	Positive photoresist

## Chapter 1: General introduction

In the twenty-first century neurological disorders are still impacting the lives of a large number of individuals. The outcomes of neuroscience in mind and brain functioning will tremendously influence the healthcare sector by evolving the treatments for various disorders and advancing the development of sophisticated tools to measure and control brain functions. The brain is a complex biological structure with immense computational capabilities to process information, construct sensory experiences, regulate thoughts and emotions, and control actions [1]. Brain functioning involves various cognitive processes for accomplishing simple to very complex tasks.

Understanding the biological nature of cognitive processes like: memory, spatial-navigation, decision-making and planning of complex movements will reveal new insights for the science community [1]. Distributed brain regions are interacting for computing the various cognitive processes [2].

Research to both neural circuits and individual nerve cells is necessary to advance the understanding of complex brain functioning. The power of the brain comes from the enormous amount, diversity, and interactions between the nerve cells, also known as neurons [1]. Neurons are fundamental signalling units arranged in specialized circuits for carrying out different cognitive functions of the brain [1]. One of the great neuro-technological challenges is to record the activity of thousands of neurons simultaneously to acquire more knowledge about the interaction of distributed brain regions.

Two main cellular recording techniques exist to advance the understanding of brain functioning: 1) cell imaging techniques, and 2) invasive electrophysiological recordings.

Cell imaging techniques, like calcium imaging, make use of fluorescent molecules that respond to the binding of calcium ions. At resting conditions, the calcium concentration inside a neuron is low. When the neuron becomes active, voltage gated calcium channels open and the intracellular concentration of calcium rises [3]. In this way the calcium concentration of a neuron is visualized. This enables the study of neural activity in hundreds of neurons. Calcium imaging is an indirect measurement of neural activity and generally requires the validation of electrophysiological recordings. Additionally, imaging techniques are restricted to the superficial cell layers as it is impossible to record from deeper brain regions without removing the above cell layers, which results in abundant tissue damage.

Invasive electrophysiological recordings allow direct access to the electrical signals of neurons, and therefore yield a higher temporal resolution compared to the imaging techniques [4]. Furthermore, deeper brain regions can be targeted with the least tissue damage. Invasive electrophysiological recordings can be subdivided into intracellular and extracellular recordings. Intracellular recordings provide high signal-to-noise ratio signals by penetrating the somata (cell bodies) of neurons with sharp

microelectrodes. However, long-term chronic intracellular recordings in behaving animals are not possible because small movements of the electrode inevitably damages the neuron. Moreover, it would not be feasible to record large populations of neurons simultaneously with this technique.

With extracellular recordings the electrodes are positioned in proximity of the neurons. Large electrodes are used to record field potentials that represent the summed activity of multiple neurons. With sufficiently small electrodes positioned within 100  $\mu\text{m}$  of the cell body, single action potentials of nearby neurons can be recorded, in addition to the field potential. For isolating a large number of neurons, an array of electrodes is required, which enables the classification of action potentials according to their neuronal source using spike sorting algorithms. Such arrays either consist of a large group of metal wire electrodes or an array of electrodes embedded onto a probe [5].

By implanting a probe into an anaesthetized animal no information is obtained about the cognitive processes that are executed by the brain. If an animal can behave but restricted, a lot more information can be obtained about the cognitive processes. To study the most complex processes in the brain, a free behaviour of the animal is required. In this way there are fewer limitations on the behavioural task that can be executed.

Studies of neural activity in freely behaving animals are indispensable to understand how the brain performs computations and supports cognition [6, 7]. Knowledge about neural circuit functioning is enhanced by long-term electrophysiological recordings of large populations of neurons in freely behaving animals [8]. Essential tools for an experimental setup are a data acquisition system, signal processing software, and an advanced brain implant to support large-scale monitoring of neural activity in freely behaving animals, see figure 1.

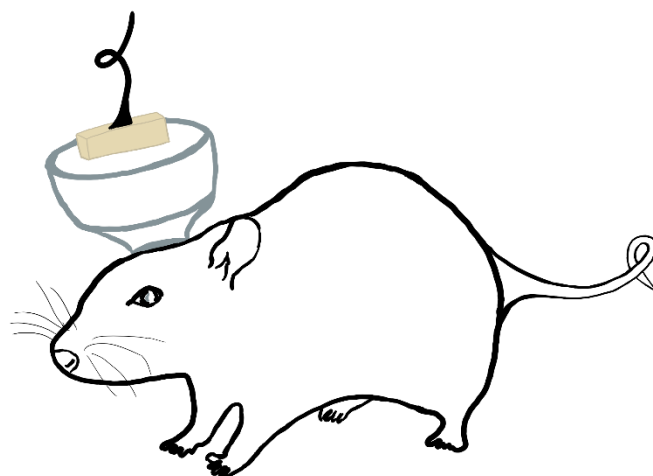


*Figure 1: Freely behaving rat carrying a brain implant on its skull*

## 1.1 Brain implant for advancing the knowledge about memory functioning

The aim of this thesis is to develop a new generation of brain implants that will be used to study in detail the processes of decision making and memory formation. Decision making involves a biological understanding of the mind and can be interpreted as a sequence of operations implemented by the brain [1]. Memory is the ability to acquire and store information of daily life activities, and also of complex and abstract knowledge [1]. Neural circuits related to decision making and memory formation are found in the hippocampus and adjacent brain regions [2, 9]. Those brain regions interact with each other to support the acquisition and storage of new information.

A cognitive map within the hippocampus generates the absolute space and forms a neural system providing the basis for an integrated model of the environment [10]. The cognitive map contains a place system which consolidates spatial relations between places in the organism's environment and the existence of unique objects in those specific places [10]. Place fields are spatial locations in an environment that correlate with firing place cells [2, 6]. A place cell is a neuron that is active when a specific place is entered within the environment. Neuroscience to the firing of place cells within specific places advances the understanding about decision making and memory functioning.

A brief explanation about the targeted anatomical structures is given. The brain consists of the cerebrum, brainstem and cerebellum, and is protected by the skull [11]. The cerebrum is the largest part of the brain and is divided into two hemispheres, both consisting of an outer layer of grey brain matter and a core of white brain matter [11]. The hippocampus is a deeply located structure within the cerebral cortex and is present in both hemispheres. It includes two interlocking parts, the hippocampus proper and the dentate gyrus (DG), see figure 2. The hippocampus proper consists of three subfields: Cornu Ammonis (CA) 1, CA2 and CA3. A densely packed layer within the hippocampus, known as the pyramidal cell layer, contains pyramidal cell bodies (somata) which are signalling units associated with memory [12, 13]. The pyramidal cell layer is the targeted region for electrophysiological experiments related to memory.

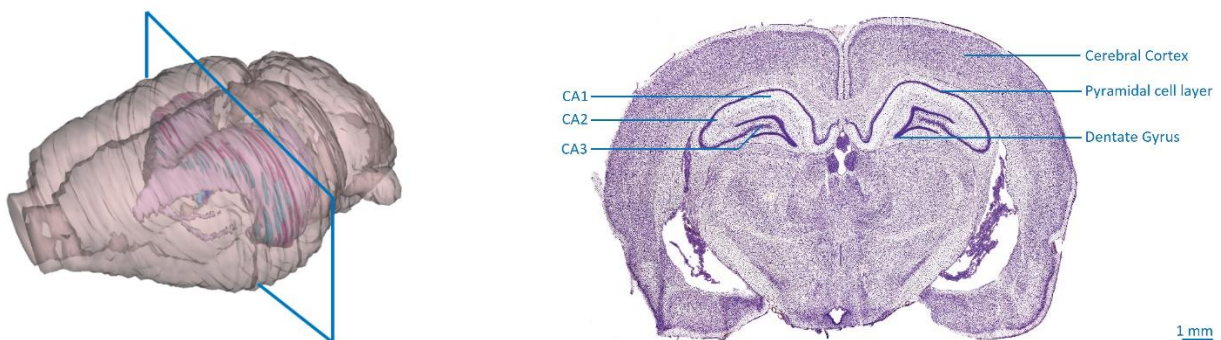


Figure 2: 3D model and slice of a rat's brain [14, 15]. The slice is located 3.96 mm posterior to Bregma and shows the dentate gyrus and the hippocampus CA1, CA2, and CA3 region.

## 1.2 Thesis objective

The goal of this thesis was the development of a next generation brain implant for distributed recordings of cellular activity in freely behaving rodents. The brain implant, see figure 3, contains two main components: 1) the probes for recording the electrophysiological signals, and 2) the holder necessary for lowering the probes to the target location in the brain.

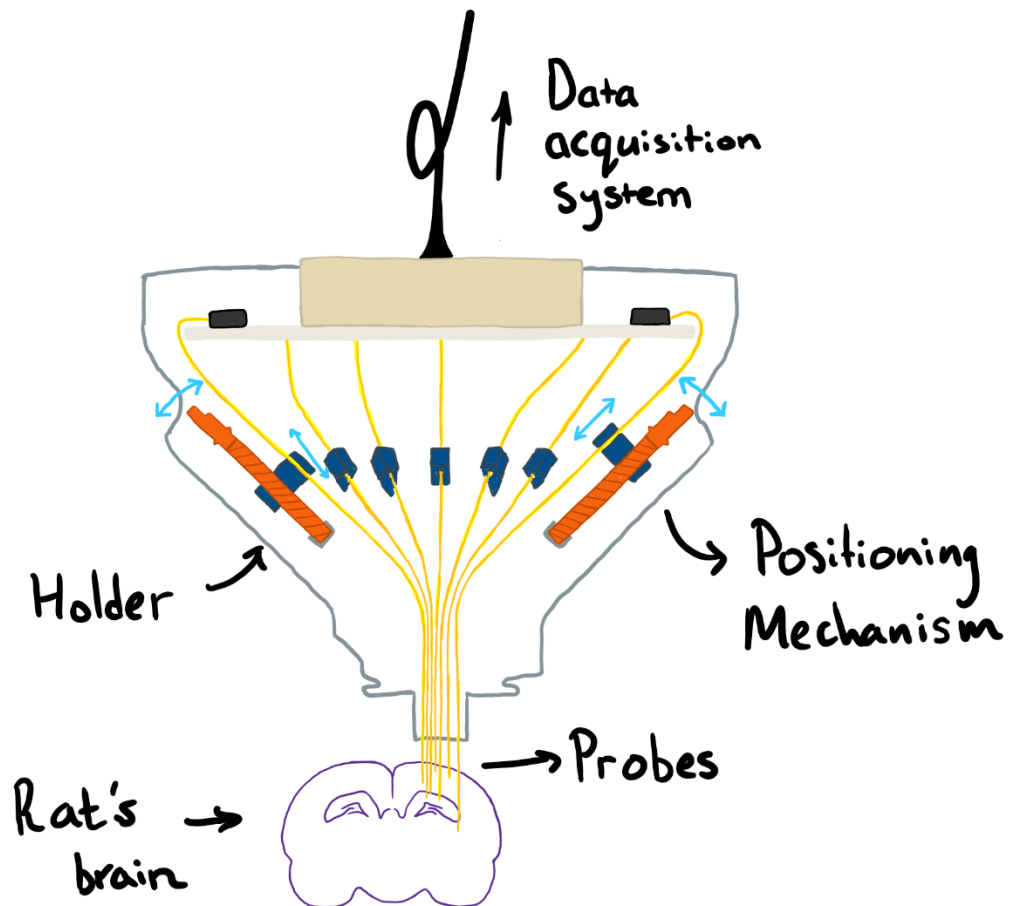


Figure 3: Cross-section of the conceptual drawing of the next generation brain implant. The probes are lowered into a rat's brain by a positioning mechanism and will record electrophysiological signals that are delivered to the data acquisition system.

The novel brain implant should feature a simple assembly, must be reusable and adequately register cellular activity over an extended time period (weeks). Additionally the brain implant must be robust to protect all its electronic components from the rat's movements and extended experimental handling. The brain tissue should remain as intact as possible, therefore the width cross-section of the probe should be as small as possible. The brain implant itself will influence the natural behaviour of the subject. Therefore, the size and weight of the implant should be minimized to have the least interference with the natural behaviour. Otherwise considerable physical stress is exerted on the animal which may influence its performance to complete a complex behavioural task [16]. To incorporate all these requirements a diverse spectrum of production processes was applied, ranging from 3D-printing techniques to micromachining technology.

The new brain implant for performing electrophysiological experiments contains a considerable number of innovations. Sixteen flexible polyimide probes with each sixteen recording electrodes are included into the brain implant. The brain implant was able to detect single action potentials of neurons in the pyramidal cell layer of CA1.

The remaining part of the thesis is divided into the following chapters. Chapter 2 discusses the developed probes to record the electrophysiological signals from the rodent's brain. First the different variants of brain recording electrodes are discussed, hereafter the developed solution is given. In chapter 3 the probe positioning mechanism (hyperdrive) is explained. There it is clarified how an array of flexible probes is lowered into the targeted brain area and still maintain a freely behaviour of the rat. Chapter 4 describes the validation methods for the probes and hyperdrive. The final chapter will discuss the entire thesis project.

## Chapter 2: Flexible polyimide probes

*Flexible polyimide probes with platinum electrodes were manufactured to record electrical signals from a rodent's brain. This chapter describes the design preferences, production process and outcomes of the flexible polyimide probes. The probes were designed with Virtuoso<sup>1</sup> and produced by micromachining techniques within Leuven NanoCentre<sup>2</sup>. First an introduction is given about the different types of recording electrodes.*

### 2.1 State-of-the-art

The first microelectrodes used for single neuron recordings were made of glass, filled with an electrolytic solution, see figure 4A [5]. As long-term *in-vivo* electrophysiological experiments required stronger and more conductive electrodes, metal electrodes were consequently developed [5]. A substantial invention by O'Keefe and Bouma in 1969 was the formvar-coated nichrome wire with the recording site located at the tip [5]. O'Keefe and Bouma were the first neuroscientists using such wires to perform electrophysiological experiments. Many research groups would later implement the use of metal electrode wires.

The stereotrode was introduced by McNaughton in 1983 and consists of two 20  $\mu\text{m}$  thick polytetrafluorethene (PTFE/Teflon) insulated platinum-iridium wires fused together and cut transversely, see figure 4B [5, 17]. The major benefit of the stereotrode was that the two electrodes picked up the same spike waveform, but with different amplitude [5]. The spike amplitude depends on the distance of the neuronal source to the two wires. The spike amplitudes are then plotted on different axes, i.e. a 2D-projection used to separate the spiking activity of a neuron from the spiking activity of neighbouring neurons [5] [18]. When two additional wires are added to the stereotrode to further improve cell separation, the recording device is named a "tetrode", see figure 4C. Electrode wires are often made of a nichrome core with a formvar coating and fused together by a heat gun. The total outer diameter of a tetrode is approximately 40  $\mu\text{m}$  [5]. The recording sites of the tetrode are plated with gold to reduce the electrical impedance for creating a stable electrochemical interface between electrode and tissue. Tetrodes are widely used tools for large-scale recordings of single unit activity in the hippocampus [5, 19], as the close proximity of the electrodes to the cells improves the quality of spike sorting [20]. While there is a rising demand for simultaneous distributed recording of neural activity, further increasing the number of electrodes by adding more wires to the tetrode is challenging [21]. Moreover, tetrodes are handmade making it a labour-intensive process if a large number of wires is needed. Reproducibility of a handmade process is also a concern and will add

---

<sup>1</sup> Custom integrated-circuited (IC) design software by Cadence Design Systems, San Jose, California, USA

<sup>2</sup> Leuven NanoCentre is a research facility of the KU Leuven, which possesses over a state-of-the-art cleanroom

variability to the quality of the recordings. Another downside of the tetrode is that the recording sites are located on the tip: If the wire is pushed through the targeted cell layer, electrophysiological recordings become more difficult to perform. Retraction of the tetrode will not help as the neurons are already penetrated and destroyed by the tetrode itself.

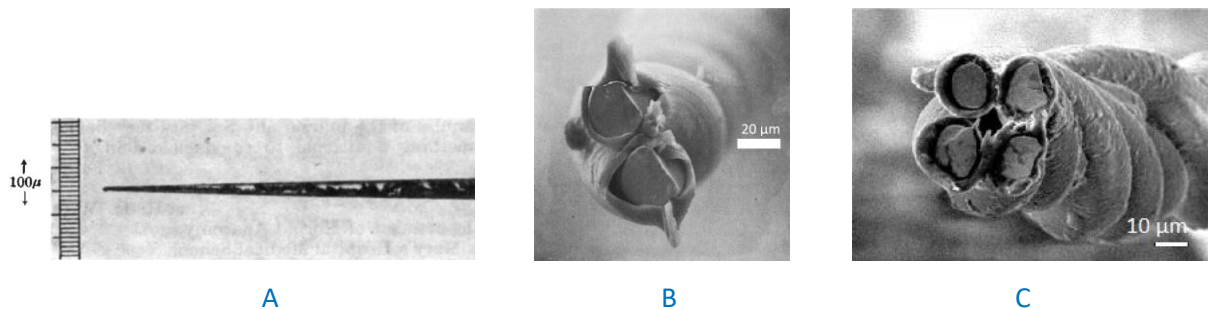


Figure 4: Overview of the various electrode wire inventions. A) Metal electrode within a glass capillary [22] B) Stereotrode, made of two teflon coated platinum-iridium wires [17], C) Tetrode consists of four bundled formvar coated nichrome wires [23]

Compared to traditional wire electrodes, the recording site configuration of micromachined silicon probes is defined with high precision by photolithography [24], see figure 5. The recording electrodes can be arranged into geometric patterns with a very narrow pitch or more than hundred micrometres apart, enabling more dense or distributed recordings, respectively. The well-arranged configuration helps researchers to infer the spatial organization of neurons [20]. Probes are usually designed with a needle-pointed tip to easily penetrate the tissue and minimize tissue damage during insertion [20].

The disadvantage of rigid silicon probes is the mechanical mismatch with the soft brain tissue (approximate Young's moduli are 170 GPa and 3 kPa, respectively) [24]. Due to continuous brain movements and the mechanical mismatch an inflammatory reaction can be triggered [21, 24], leading to glial scar formation around the foreign material that isolates the probe electrically from the surrounding tissue [24]. Long-term electrophysiological recordings cannot be carried out if the glial scar forms a thick layer. Therefore, it is crucial to minimize the host response and hence, reducing the formation of glial scar tissue. The brain tissue is supplied by oxygen and energy holders, like adenosine triphosphate, through a network of blood vessels. Proper brain functioning is only guaranteed when the blood vessel network remains as intact as possible. Host response and tissue damage are important criteria that should be minimized for the entire recording period, and are crucial aspects for the new brain implant design. Both criteria can be minimized by reducing the cross-sectional area of the probe and by using flexible materials, such as polyimide, that move in unison with the brain [21, 24]. Favourable properties of polyimide include biocompatibility, insulation resistance, dielectric strength, and mechanical flexibility [24]. Polyimide probes can bend in acute angles without breaking the electrode lines, which is advantageous for *in-vivo* applications when compared to the fragility of silicon recording electrodes [24]. One challenge with flexible polyimide probes, however, is the insertion into

the brain tissue, since the probes can bend during the process. This is often solved by using: a biodegradable coating [21], stiffeners [25, 26], backbone [27] or delivery tool [28]. When using a bioabsorbable coating the electrode can be brought in place, but later manipulation becomes difficult. When using stiffeners or delivery tools the tissue damaged area is larger than if the probe would be inserted solely. A backbone might stiffen the probe too much, and the unison movement with the brain is restricted.

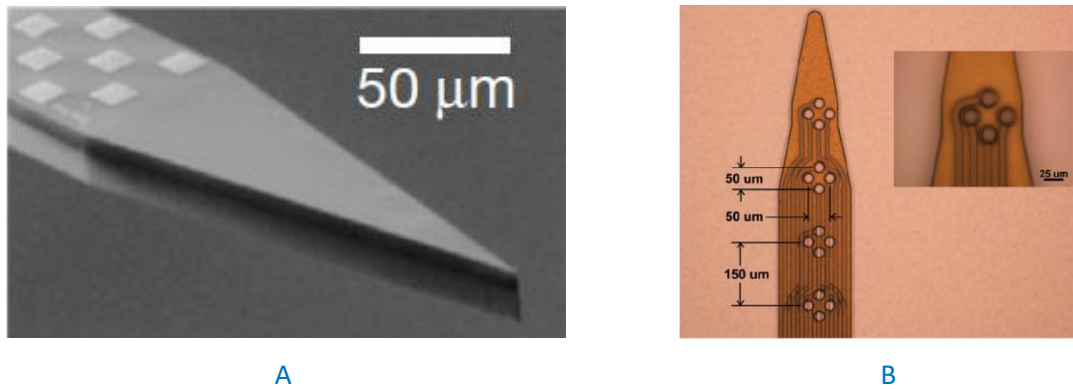


Figure 5: Probes showing patterned electrode configurations. A) Silicon probe with a high defined pattern by photolithography [29], B) Polyimide probe with a tetrode configuration for single-unit sorting [30].

The present criteria for probe development are: 1) low electrical impedance for the maximization of the signal-to-noise ratio, 2) small electrodes with small inter-electrode distance for isolating single neurons, 3) match to the mechanical properties of brain tissue, 4) biocompatibility, and 5) long-term stable recordings [5].

## 2.2 Design phase

The new flexible probes were designed with respect to the design requirements and limitations of the fabrication process, see table 1. Previous production processes at Leuven NanoCentre showed that a pitch of 6.5 μm was the minimal achievable pitch for the current fabrication process.

Table 1: Design requirements and specifications of the flexible probes. The total probe width is determined by the electrode configuration and calculated with equations (2.1 – 2.4).

Requirements	Symbols	Values
Length of entire probe	$L_{probe}$	58 [mm]
Electrode diameter	$\varnothing_{electrode}$	15 [μm]
Extra required diameter for undercutting	$\varnothing_{extra}$	2 [μm]
Line width	$w_{line}$	2.5 [μm]
Spacing	$w_{spacing}$	4 [μm]
Additional spacing at probe edges	$w_{extra}$	8 [μm]

The total width of the probes is a summation of the total electrode width, the line width and the total spacing:

$$W_{probe} = w_{electrodes} + w_{lines} + w_{spacing} \quad (2.1)$$

$$w_{electrodes} = \#_{electrode\ columns} * (\emptyset_{electrode} + \emptyset_{extra}) \quad (2.2)$$

$$w_{lines} = ((\#_{electrode\ columns} * \#_{electrode\ rows}) - \#_{electrode\ columns}) * w_{line} \quad (2.3)$$

$$w_{spacing} = ((\#_{electrode\ columns} * \#_{electrode\ rows}) + 1) * w_{spacing} + w_{extra} \quad (2.4)$$

Each probe contains 16 recording electrodes because adding more electrodes would make the probes too wide. The probes are provided with connector pads whereof the pitch is adapted to a 16 channel zero-insertion-force (ZIF) connector.

The hippocampal pyramidal cell layer is a thin layer, and so to enable spike sorting it is convenient to use a dense array of electrodes. Two electrode arrays were designed for this purpose: a 3x5+1, and a 4x4 electrode configuration, columns and rows respectively, see figure 6. The 16<sup>th</sup> electrode in the 3x5+1 design is located 400  $\mu\text{m}$  above the central electrode and used as a reference, as it will sit in an electrically quiet cell free brain region. For cortical cell recordings, i.e. thicker cell layers, it is more appropriate to increase the recording channels along the length direction of the probe. A 2x8 and 1x16 design were made so that adjacent brain regions can be targeted simultaneously, e.g. several layers of the cortex.

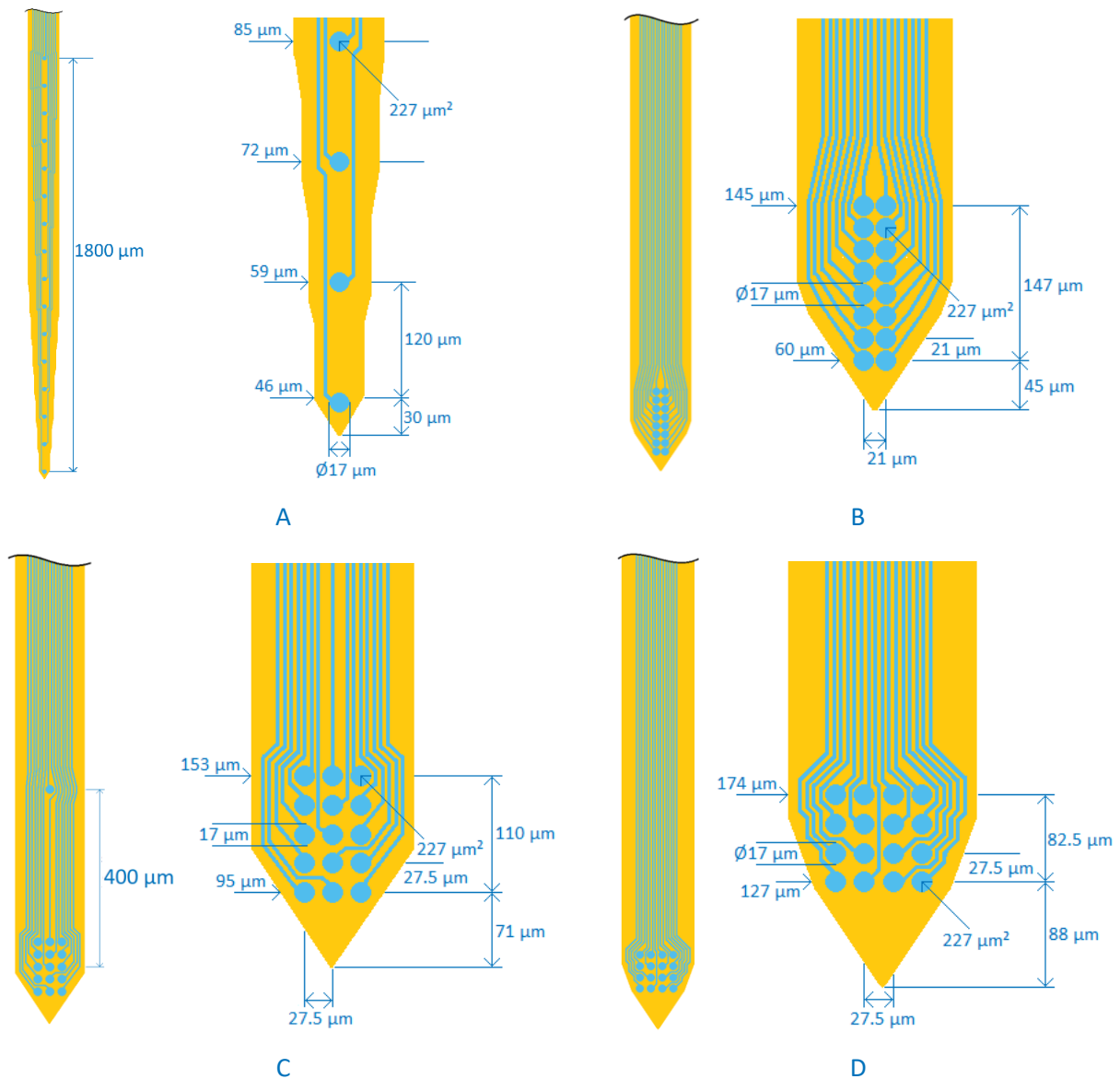
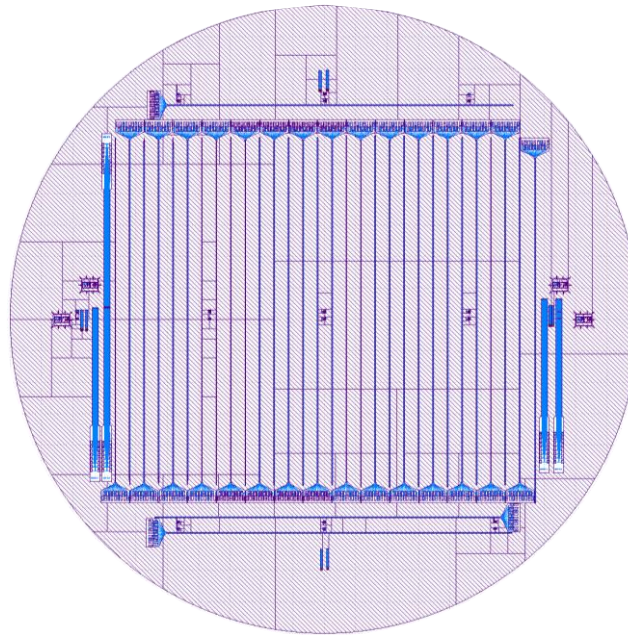


Figure 6: Designed probe configurations. A) 1x16 configuration, B) 2x8 configuration, C) 3x5+1 configuration with reference at 400 μm, and D) 4x4 configuration. Designs C and D are more appropriate for recording from the pyramidal cell layer, while designs A and B are more applicable for recording from the cortex.

Equations 2.1 to 2.4 show that the total width of the probe is determined by the number of electrode columns, since the pitch, line width and spacing, remains constant for the different probe designs.

The probe designs are formed by two materials, one is the conductive paths, and the other the probe body. The electrodes are drawn as circles and the lines by connecting rectangles together. By connection two straight lines with a diagonal line, two mirrored triangles should be drawn to form a parallelogram with the correct line width. Because when two lines are connected together by a polygon the line width is reduced and problems might occur in the production process.

The probe designs were added on a virtual wafer, see figure 7. Alignment marks were added for aligning the different layers, this is further discussed in the fabrication process. Test structures were also included to check the etch quality and conductivity of the lines.



*Figure 7: Virtual pattern on a 4" wafer with the different probe designs. This file is used for the production of the photo masks.*

### 2.3 Method

Micromachining technology was the applied technique to produce the flexible polyimide probes. During the entire production process, it is important to keep the wafer as clean as possible, as contaminations will reduce the end-quality of the probes. To reduce the amount of contamination, the probes were made in special cleanrooms. The purity of the air is determined by the ISO-class of the cleanroom<sup>3</sup>. The most considerable source of contamination are the operators itself, which need to wear special suits to avoid such contamination.

Micromachining technology can be divided into three subgroups: 1) deposition of layers, 2) photoresist patterning by photolithography, and 3) etching the deposited layers [31]. The applied production method is now briefly described.

A silicon wafer was used as a carrier for producing the polyimide probes. First, a thin layer of aluminium was evaporated onto the wafer that serves as a sacrificial layer. Next, a layer of polyimide was spin-coated and cured. A lift-off resist layer was deposited on top of the polyimide, followed by the deposition of a photoresist layer, which was patterned by photolithography and developed. Platinum was deposited by sputtering and evaporation and patterned by lift-off to form the electrodes,

<sup>3</sup> Leuven NanoCentre features an ISO 6 class cleanroom which is equal to one million 0.1  $\mu\text{m}$  particles/ $\text{m}^3$ .

connectors and connection lines. A second layer of polyimide insulates the lines and covers the entire structure. An aluminium mask layer was deposited and patterned by photolithography. The electrode and connector sites are opened along with the probe outline using dry etching. Finally, the probes are released from the silicon substrate by etching the sacrificial layer. The complete production process will be discussed in more detail in section 2.5. First an overview will be given about the used materials and encountered problems during the production process.

## 2.4 Materials and determination of process parameters

In total 28 wafers were used for testing, optimizing and fabricating the flexible polyimide probes. The detailed results for each wafer can be found in appendix B.

The metal tracks are defined by photolithography, which is the process to pattern the thin film. A two-layer resist was used for improving the resolution of the metal tracks. The first layer is a lift-off resist for lifting off the excessive metal, the second layer is a photoresist which enables photosensitivity. This two-layer resist combination is used to create an undercut profile underneath the top layer, preventing fencing of the metal deposited on top and subsequently the metal is patterned by lift-off. Fencing is the deposition of metal onto the side walls of the undercut profile.

Two different lift-off resists were tested, a more viscous resist LOR10B and a more fluidic resist LOR3A. The viscosity and spinning speed determine the thickness of the resist layer. After spinning, the resist is baked and developed. It is important that the resist is correctly developed, and if not two problems might occur, see figure 8. If the development time is too short, the lift-off resist might not be completely developed, and stay on top of the polyimide, resulting in complete lift-off, see figure 9a. If the resist is too long developed, the resist layers detach from the substrate, see figure 9b. The viscous resist LOR10B was better controllable and resulted in a proper lift-off.

For each wafer the positive photoresist S1818 was applied at a spinning speed of 4000 rpm and baked for 2 min at 100 °C. For the development of the resist layers 2.5 L of 4:1 concentrated 351 solution was made, so only minor errors are introduced and a constant concentration is assumed for all separate wafer developments. For each development exactly 80 mL of development solution was taken to have the least influence.



*Figure 8: Illustration of resist development problems. The lift-off resist is shown in green. A) The lift-off resist is not developed long enough causing a lift-off of all deposited metals. B) Too long developing causes drift of the top resist layer or a fusion of the metal tracks later on.*

Several problems were encountered during the metal deposition. When sputtering is used for the deposition of platinum and iridium oxide, a significant amount of debris particles remained between the lines after lift-off. This is visualized by inspections with a bright field and scanning electron microscope (SEM), see figure 10. Metal particles between electrode lines are to be avoided as those can form short-circuits between the different electrodes, resulting in shorts or cross-talk.

To remove the debris particles, the wafers were placed in an ultrasonic bath for 3 min with a visual inspection after each minute. It was noticed that some particles remained, forming interconnections between lines. Longer ultrasonication times are not recommended as the metal lines can detach, see figure 11.



Figure 9: Possible problems that can occur with lift-off. A) All metal paths are lifted-off from the substrate. B) The resist was too long developed and loosened from the substrate. In this case the metal tracks would fuse together when depositing.

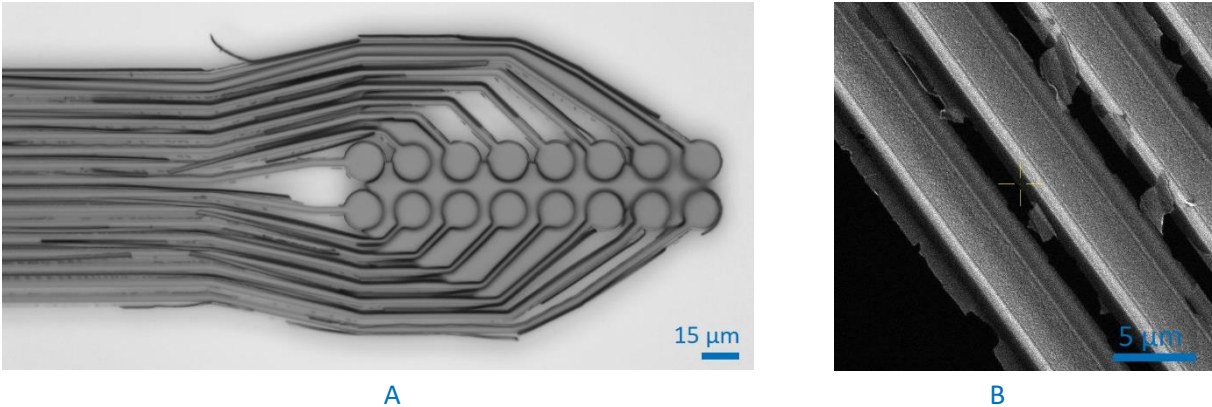


Figure 10: Debris particles between the electrode lines. A) Inspection of the probe with a bright field microscope, resist and debris particles remained between the lines. B) Inspection with the scanning electron microscope: debris in between the lines allows current to pass, producing cross-talk.

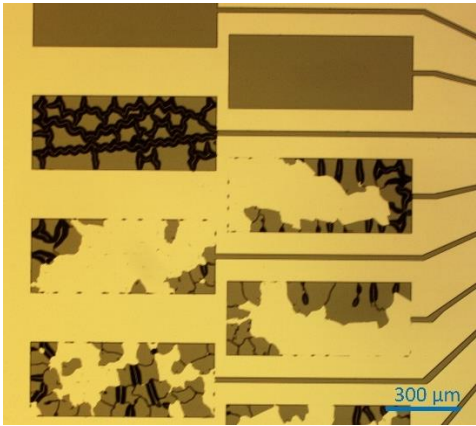
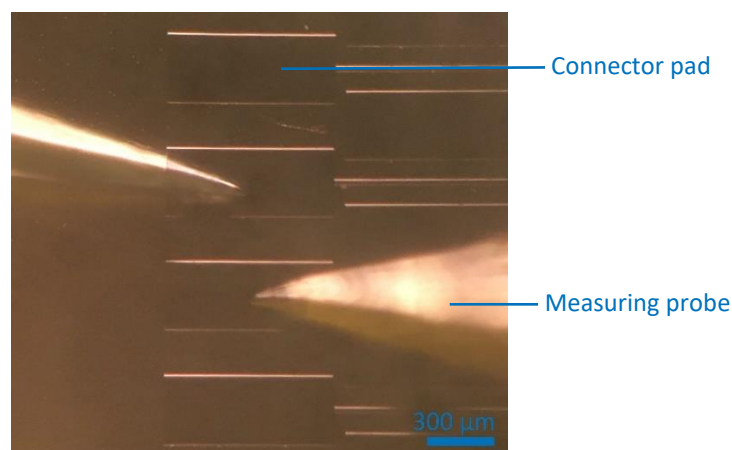


Figure 11: The deposited metal connector pads are loosened by the ultrasonic bath.

An alternative removal solution is dissolving the metal particles. The wafers were placed in 50 °C heated aqua regia for 5 min to dissolve the particles. Aqua regia is a 3:1 molar concentration of hydrochloric acid (HCl, 6mol/l) and nitric acid (HNO<sub>3</sub>, 65%), and is used to etch noble metals like gold and platinum [32]. However, this solution might not be ideal as aqua regia can introduce artefacts by etching away the metal lines itself.

When the probes appeared to be clean, the result was validated by an impedance measurement between the different electrode paths. A probe station, digital multimeter and external voltage source were used to perform the test. The probe needles were placed on adjacent bond pads, see figure 12. An external voltage source was used as otherwise a breakdown voltage would occur between the paths due to the small pitch. Unfortunately, impedance values between 10.0 kΩ and 178kΩ were found, which indicate that interconnections were still present between the different paths. For isolated paths resistance values in the MΩ range are expected. The above results indicate that the lift-off process did not work properly and that the applied methods to remove the particles were not satisfying.



*Figure 12: Measuring probes on two adjacent connector pads to determine cross-talk. Impedance values indicate that interconnections between tracks are present. This disables single-cell sorting as the waveforms of the electrodes will be the same.*

It was found that the debris particles were formed by the sputtering process itself, as the side walls of the lift-off resist are also covered by the sputtered metal in an indiscriminate way, called fencing. Therefore, the lift-off resist could not be removed sufficiently, forming interconnections between the lines. To overcome this problem, a two-step metal deposition method was introduced: an initial sputtering step and an evaporation step. The sputtering step is necessary for a strong adhesion to the polyimide. Evaporation is more directive and will yield a better lift-off. The metal deposition was performed exclusively with platinum, as evaporating iridium requires very high temperatures that might damage the photoresist layers. Based on the exploration of process parameters the final fabrication process is given below.

## 2.5 Fabrication process

The final fabrication process of the flexible polyimide probes will now be discussed in detail. Supportive figures were added and the fabrication sequence is clarified by cross-sections in figure 13.

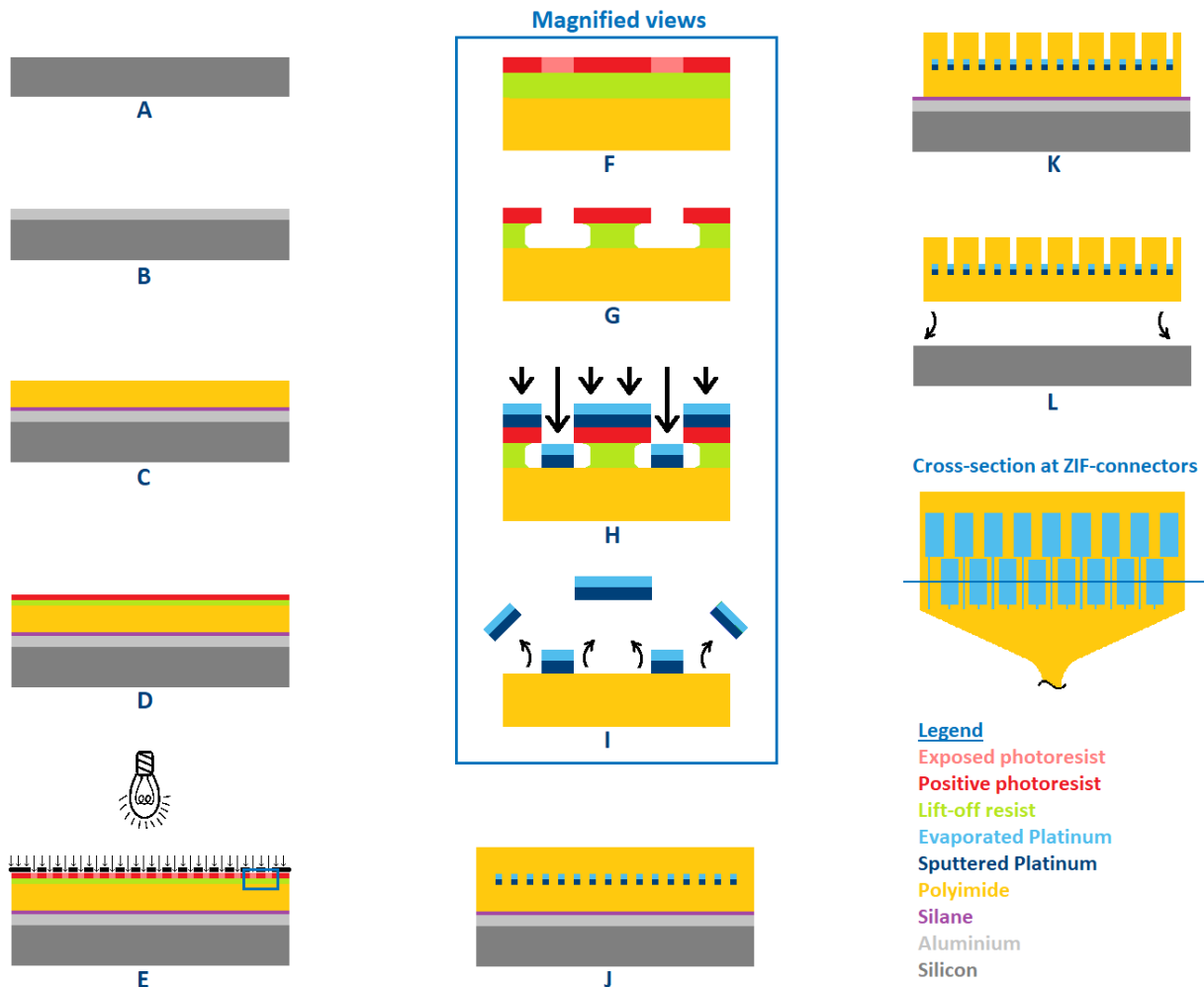


Figure 13: Fabrication sequence of the polyimide probes. The width cross-section is shown on the right together with the legend. A) Silicon wafer, which is used as a carrier and will not be part of the probes, B) Sacrificial layer of evaporated aluminium, C) Adhesion promoter silane<sup>4</sup> and spin-coated layer of polyimide D) Spin-coated lift-off and photo-resist layers E) Exposure of the photoresist layer through a photomask F) Detailed view showing the polyimide base with two-layer lift-off resist. The resist is illuminated according to the pattern of the photomask, G) The developed resist layers, the lift-off resist develops isotopically and form an undercut, H) Ideal representation of a dual-layer platinum deposition by sputtering and evaporation, I) Lift-off process, the resist layers are dissolved and lift-off of the excessive metal. J) Second spin-coated polyimide layer, K) Contouring and opening of the electrode and connector holes, L) Etching the sacrificial layer which releases the probes.

<sup>4</sup> VM-651 Hitachi Dupont (HD) MicroSystems

### 2.5.1 Wafer and cleaning

Four inch single side polished <100> crystal oriented silicon wafers<sup>5</sup> were used as carriers to produce the flexible polyimide probes, i.e. the silicon will not be part of the probes, see figure 13A. The silicon wafers were engraved on the backside by a diamond tool for tracing during the entire fabrication process. The silicon surface oxidizes upon exposure to oxygen, also known as the native oxide layer. The native oxide layer was removed by immersing the wafer into 7:1 buffered hydrofluoric acid (HF:NH<sub>4</sub>F) for one minute [31]. It is highly recommended to remove the native oxide layer as silicon dioxide is very inert and hence, it acts as a protective layer that prevents chemical reactions with the underlying silicon [31]. Removing the native oxide layer will improve the adhesion with the upcoming aluminium layer.

It was checked if the native oxide layer was completely removed by spraying high-purity water (18 MΩ) onto the silicon surface, were a hydrophobic reaction to the water occurred, see figure 14. The wafer was blown dry by pressurized nitrogen gas with a 99.9999% purity<sup>6</sup>. Nitrogen is used because it is an inert gas that is cleaner and drier than air and will not react with the substrate.



*Figure 14: Silicon wafer with water droplets. A hydrophobic reaction to the substrate surface appeared, which indicates that the native oxide layer was sufficiently removed by buffered hydrofluoric (HF) acid.*

### 2.5.2 Evaporation of the sacrificial layer

A sacrificial layer is a deposited layer which is later removed for creating cavities or releasing structures [31]. For this project a sacrificial layer is used to release the flexible probes from the silicon wafer. The sacrificial layer is composed of aluminium that is deposited by evaporation<sup>7</sup> onto the cleaned silicon substrate, see figure 13B. In the final production step the aluminium layer is etched to release the probes, see figure 13L.

Evaporation uses a vacuum chamber and tungsten coil with an aluminium coating, see figure 15 . Evaporation requires a high vacuum to enable direct travelling of the particles to the substrate without interacting with the background gas. Evaporated aluminium atoms that collide with a gas may react.

---

<sup>5</sup> Siltronic, Munich, Germany

<sup>6</sup> N60, Air Liquide, Paris, France

<sup>7</sup> Balzers Med 010 evaporation tool

For example when aluminium is evaporated in the presence of air, aluminium oxide is formed instead. Electric current is applied through the tungsten coil, generating heat which evaporates the aluminium. This aluminium vapor then condenses onto the substrate as a thin film [31].

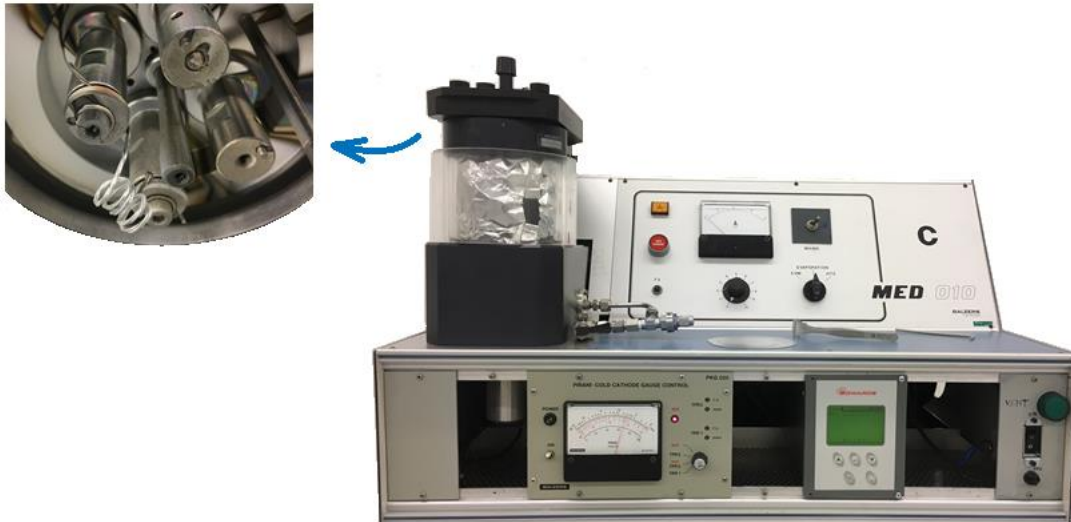


*Figure 15: Balzers Med 010 evaporation tool. The machine includes a vacuum chamber, pressure gauge and controls for regulating the current. Left a view is given from within the vacuum closing lid. A current is passed through the aluminium coated tungsten coil to form thin films of aluminium.*

### 2.5.3 Polyimide deposition

Spin-coating is frequently used to form thin films of organic material. A fluid material is applied onto the centre of the substrate, which is rotated at high speed, spreading out the material by centrifugal forces and coating the substrate. The thickness of the thin film is determined by the spinning speed and viscosity of the coating material.

First a layer of silane VM-651<sup>8</sup> was applied, see figure 13C for improving the adhesion between the inorganic aluminium layer and upcoming polyimide. The silane coupling agent contains an organofunctional group for bonding to the polyimide and a hydrolysable group that forms silanol (SiOH) groups in aqueous solutions [33]. The OH-groups provide the adhesion between the aluminium and the upcoming layer of polyimide. Silane at a concentration of 0.1% was spin-coated at 3000 rpm for 30 s and baked at 110 °C to evaporate the adsorbed water.

Polyimide PI-2611<sup>8</sup> is spin-coated<sup>9</sup> at 2033 rpm for 30 s, to obtain a 7.5 µm thick polyimide layer. Next, the wafer is pre-baked by placing it on a hot-plate at 90 °C for 1 min and, gradually heated until 150 °C and left at that temperature for 1.5 min. Hereafter, the wafers were placed in an oven and baked at

<sup>8</sup> Hitachi Dupont (HD) MicroSystems

<sup>9</sup> POLOS 200 spin coater

200 °C to further cross-link the polyimide chains, see figure 16. Full cross-linkage is not yet desired as later a second layer of polyimide needs to adhere to the substrate.

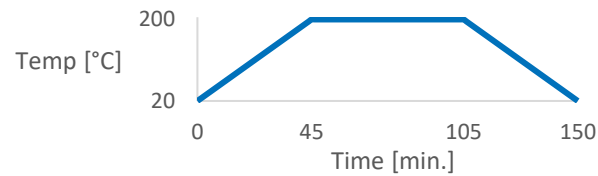


Figure 16: Pre-baking temperature profile for polyimide.

#### 2.5.4 Photolithography and mask development

Photolithography is the process applied for patterning the metal tracks, see figure 13D-G. The benefit of using photolithography instead of a pattern generator is the fast optical exposure:  $10^{10}$  pixels can be illuminated in less than 1 second through a photomask [34]. The production procedure of the mask will be briefly explained. The photomask material is made of transparent borosilicate glass with a 100 nm thick opaque chromium layer, anti-reflective coating of chromium oxide and a 530 nm thick AZ1505 photoresist layer [35]. A beam writer, see figure 17, imprints the virtual pattern, see figure 7, in the photoresist layer of the photomask with an accuracy of 2  $\mu\text{m}$ .

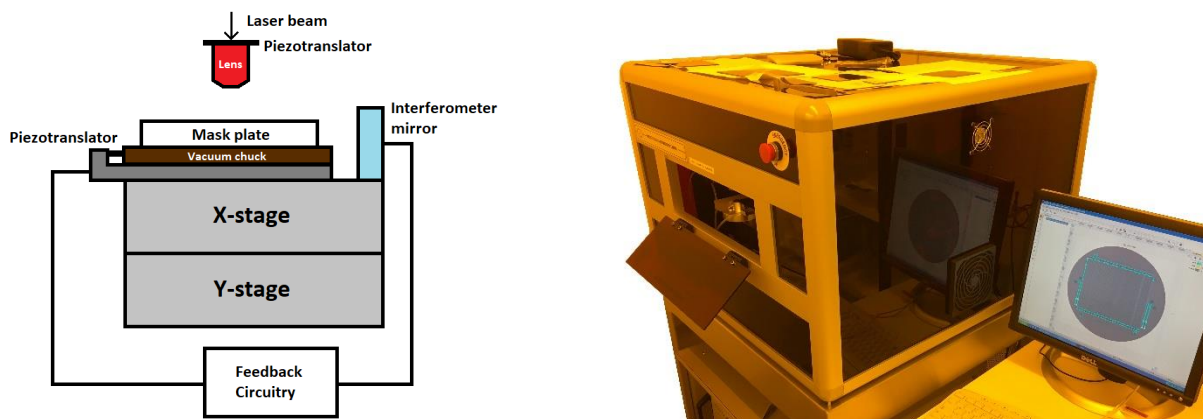


Figure 17: Laser mask writer. The laser exposes the photoresist on the photomask according to the virtual pattern. Schematic of the principle, the stages move the mask [34]. Yellow light is used in the photolithography section of the clean room because photoresists are sensitive below a 450 nm wavelength [34].

The photoresist was immersed for 3 min in 3:1 351 developer in a dilution with deionized water. The developed photoresist was inspected under the optical microscope. The chromium was etched with chromium etchant cr-14<sup>10</sup>, which is a concentration of 22% ceric ammonium nitrate  $(\text{NH}_4)_2\text{Ce}(\text{NO}_3)_6$ , 8% HAc in  $\text{H}_2\text{O}$ . Hereafter the photoresist layer on the mask was stripped by reactive ion etching (RIE). RIE will be described in more detail later when describing the etching of the polyimide layers.

<sup>10</sup> VWR Chemicals, GPR Rectapur

Photolithography comprises three subsequent steps: 1) Spin-coating of a photoresist layer, 2) optical exposure to print the photomask image onto the photoresist, and 3) the development of the exposed photoresist to render visible the latent image [31].

A two-layer lift-off resist was used for improving the resolution of the metal tracks as shown in figure 13D. The bottom resist, lift-off resist (LOR10B<sup>11</sup>), was spin-coated at 3500 rpm and baked for 5 min at 180 °C to obtain a 900 nm thick layer [36]. When developing the LOR an undercut profile underneath the top photoresist is created to prevent fencing of the metal to the side walls. If no undercut is present, the upcoming metal layer would adhere to the side walls, causing an inadequate lift-off. The top resist layer, positive photoresist S1818, was spin-coated at 4000 rpm and baked at 100 °C for 2 min to obtain a 1.8 µm thick layer [37]. The main function of the positive photoresist is enabling photosensitivity as LOR is not photosensitive [34].

Contact photolithography was used for exposing the photoresist layer, a pressure of 2 bar was applied between the mask and substrate. The photoresist is optically exposed with a dose of 23 mJ/cm<sup>2</sup> by a mercury arc lamp which irradiates UV-light through the photomask in the exposure tool. The exposure tool is again used to align the substrate and mask, therefore it is also named 'mask aligner'.

After exposure, the substrate is immersed in 4:1 351 developer for 2 min and 25 s, dissolving the exposed positive photoresist. After the developer dissolves the illuminated S1818 the LOR is isotopically dissolved, hence leaving an undercut profile, see figure 13. This profile is required for lifting-off the excess metal in the consecutive steps. The undercut profile is clearly visible under the optical microscope by slightly raising the focus of the microscope, see figure 18.

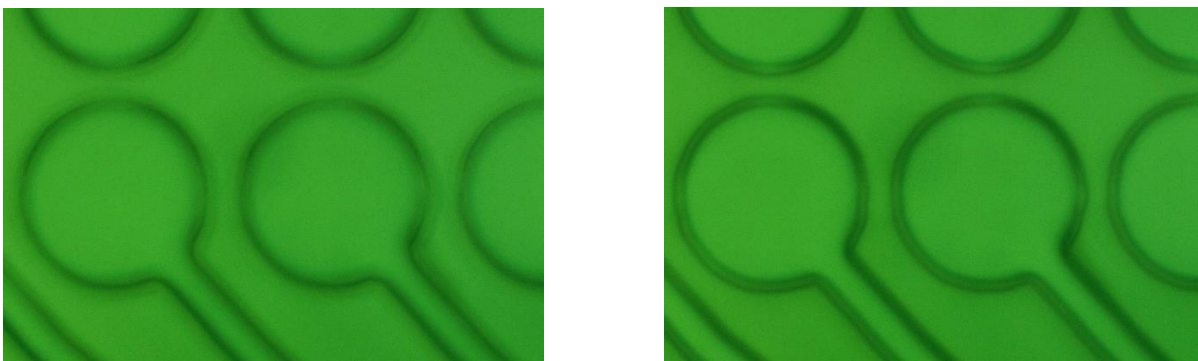


*Figure 18: Lift-off resist profile. The resist is shown through an optical microscope under green light for irradiation protection. In the left picture the top level of the resist is brought in focus. On the right picture the focus is slightly lower, an undercut is clearly visible.*

---

<sup>11</sup> MicroChem, Westborough, Massachusetts, United States

### 2.5.5 Metal deposition and lift-off

A two-step deposition method was used to improve the lift-off process, first sputtering and hereafter evaporation was applied, see figure 13H. Sputtering<sup>12</sup> uses a “target” material which is physically bombarded by a flux of argon ions in a vacuum chamber at a pressure of approximately  $1 \times 10^{-5}$  bar [31]. Radiofrequency (RF) excitation applied to the target creates a discharge in the argon background gas. A DC field superimposed onto the RF field let the argon ions bombard the target surface, releasing atoms or molecules which are deposited onto the wafer substrate [31]. Sputtering is a preferred technique for the deposition of materials at temperatures below 150 °C [31]. The physical bombardment of sputtering has more energy than in evaporation, resulting in a stronger adhesion. The random orientation of the sputtering process results in a good step coverage, which means that a uniform thin film is obtained over a geometrical step. This also means that sputtering is less directive than evaporation, which is in case of lift-off less desired. The RF source was first set at 200W for 5 s per wafer, followed by 80W for 20 s per wafer, resulting in a 20nm platinum thin film. This layer serves as an adhesion layer between the polyimide and the upcoming evaporated platinum layer. The second platinum layer was evaporated<sup>13</sup> to 80 nm thickness. In e-beam evaporation an electron beam is swept over the target material to evaporate atoms, which condense onto the substrate forming a thin film [31]. The deposition rate is controlled by a quartz crystal monitor. Evaporation is a more directive process [31] than sputtering, leaving the sidewalls exposed and hence, the lift-off process will be facilitated. The total metal thickness (100 nm) was validated with a profilometer<sup>14</sup>.

After metal deposition the wafers were immersed in N-methylpyrrolidon<sup>15</sup> (NMP) for one day to dissolve the resist layers and hereby lifting-off the redundant metal, see figure 13I. The lines were inspected under the optical microscope and the impedance was measured between the adjacent tracks. Only a few channels were interconnected so the production process was continued.

### 2.5.6 Top polyimide deposition and patterning

The second layer of polyimide, see figure 13J, was applied by spin-coating at 2250 rpm for 30 s. Pre-baked for 1 minute at 90 °C and 1.5 min at 150 °C on a hot-plate. Subsequently, the wafers were placed into an oven for baking. The temperature was increased in two stages: first to 200 °C, with a ramping rate of 4° C/min, and second to 350 °C with a ramping rate of 2.5 °C/min to fully crosslink the polyimide. At 350 °C it is important that the oven chamber is completely filled with nitrogen to prevent any

---

<sup>12</sup> Balzers BAE 370 sputtering machine, Oerlikon Balzers Coating AG, Balzers, Liechtenstein

<sup>13</sup> E-Beam Evaporation, PLS Pfeiffer

<sup>14</sup> DektakXT, Bruker, Billerica, Massachusetts, United States

<sup>15</sup> Sigma-Aldrich Emplura®, Saint Louis, Missouri, United States

reaction with oxygen. After one hour the temperature was decreased to room temperature. The temperature profile is shown in figure 19.

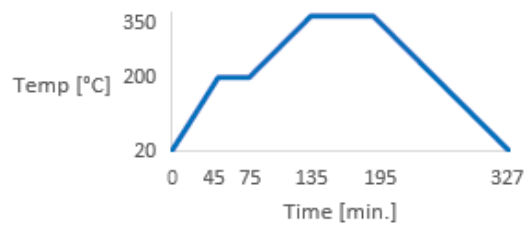


Figure 19: Post-baking temperature profile for polyimide.

At this point the entire substrate is covered by polyimide, requiring the electrode and bond-pads to be opened and defining the outline of the probe. This was done in one step, therefore reducing the cost of an extra photomask, see figure 13K. The alignment marks on the substrate were covered with tape because these are essential for the alignment with the second photomask and should not be covered with aluminium. Hereafter, a 120 nm aluminium film was sputtered<sup>16</sup> onto the substrate to serve as a hard mask when etching the polyimide with RIE. The tape was removed after the sputtering process. Hexamethyldisilazane<sup>17</sup> (HMDS) is applied for promoting the adhesion between the sputtered aluminium and the upcoming positive photoresist S1818 [34]. The positive photoresist is used for patterning the aluminium. The photoresist is applied by spin-coating at 3000 rpm for 30 s and baked at 100 °C for 2 min. A second photomask is used for patterning the structure outline, openings of the electrodes and bond pads into the photoresist layer. The exposure dose was 25 mJ/cm<sup>2</sup> with a contact pressure of 0.03 bar. The wafer was immersed in 3:1 351 developer which dissolved the exposed photoresist S1818 and aluminium after 6 min.

The polyimide layers were dry-etched with reactive ion etching (RIE). RIE uses a vacuum chamber and chemically reactive plasma to etch the deposited material. The plasma is generated by a radiofrequency (RF) powered magnetic field with a frequency of 13.56 MHz. The chamber pressure was set to 30 mTorr and the gas control to 20 sccm oxygen. The RF setpoint was 150 W. Thickness measurements were taken with a profilometer<sup>14</sup> to determine the etch rate. Herewith an estimation of the total etching time could be made, which was 70 min for 15.6 µm.

<sup>16</sup> Sputter Pod, JLS Designs Ltd, Somerton, United Kingdom

<sup>17</sup> ReagentPlus® 99.9%, Sigma-Aldrich, Saint Louis, Missouri, Verenigde Staten

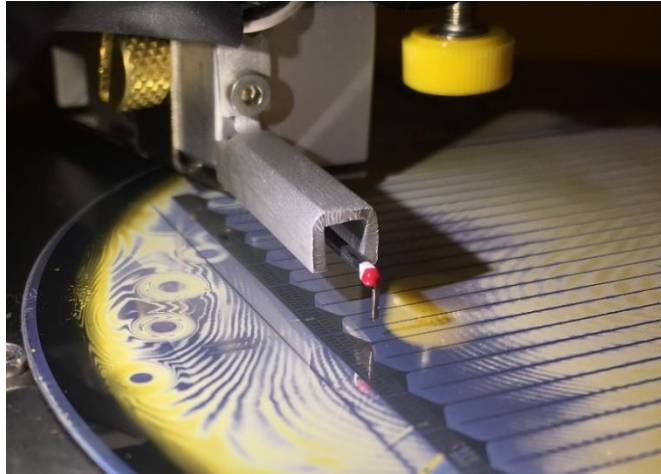


*Figure 20: Measuring the probe profile with a profilometer to determine the layer thicknesses.*

In the final step the sacrificial aluminium layer was etched in a 6:1 HCl concentration, hereby releasing the probes from the wafer, see figure 13L. The wafer was immersed for 75 min into the HCl solution.

The probes were inspected with an optical microscope and the impedance was measured between adjacent paths for checking on cross-talk. The probes were divided in three quality classes based on the previous inspections. A probe was labelled as first class if no disconnections were found nor cross-talk was measured. For the first class probes the impedances of the individual electrodes were measured with impedance tester NanoZ<sup>18</sup>. Values below 300 k $\Omega$  at 1 kHz are acceptable to acquire proper brain signals. This is further discussed in chapter 4: Validation.

## 2.6 Results

The flexible polyimide probes were created as a patterned stack of layers. The electrodes, lines and connector pads are made of platinum. The final result is shown in figure 21.



*Figure 21: Flexible polyimide probe with a 2x8 electrode configuration. The scale bar is 150  $\mu\text{m}$*

The layer heights were determined by profilometry during the production process, figure 20. The total thickness of the probes was 15.6  $\mu\text{m}$ . The height of the platinum tracks was determined directly after lift-off. The thickness of the first polyimide layer was measured as the difference between the substrate and the bottom platinum height. The thickness of the second polyimide layer was measured as the difference between the total height and the connector height, also the aluminium mask thickness was subtracted.

---

<sup>18</sup> Neuralynx, Bozeman, Montana, United States

Table 2: Features of the produced flexible polyimide probes.

Features	Symbols	Values [ $\mu\text{m}$ ]
Total thickness probe	$T_{total}$	15.6
Height polyimide layer 1	$h_{polyimide\ 1}$	8.06
Height polyimide layer 2	$h_{polyimide\ 2}$	7.54
Platinum thickness	$h_{Pt}$	0.1
Aluminium mask thickness	$h_{Al\ Mask}$	0.12
Electrode opening diameter	$\varnothing_{Electrode}$	6.42 - 7.93
Width of the 1x16 probe	$w_{1x16}$	129.5
Width of the 2x8 probe	$w_{2x8}$	144
Width of the 3x5 probe	$w_{3x5}$	151
Width of the 4x4 probe	$w_{4x4}$	172.8

Some channels were disconnected due to failures on the lines, see figure 22. This might be due to contaminations, insufficient adhesion of the metal, lift-off problems or a combination of the former.

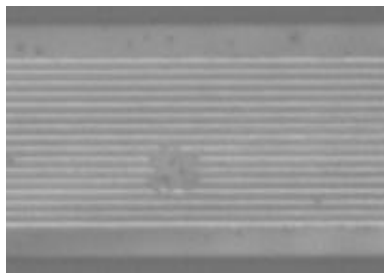


Figure 22: Line failures resulting in disconnected channels.

The insertion ability and electrical performance of the probes are further discussed in chapter 4.

## 2.7 Discussion

Four different flexible polyimide probes were manufactured with 16 recording electrodes each. The 3x5+1 and 4x4 designs are more applicable for recording from the thin pyramidal cell layer in the hippocampus, while the 1x16 and 2x8 designs are more appropriate for recording from several cortical layers. The metallization was defined by photolithography and yielded a 100 nm thick layer of platinum. The deposition method combines both sputtering and evaporation, because sputtering alone resulted in lift-off problems as was shown in figure 10. Although sputtering cannot be completely dismissed as a very thin layer of platinum is necessary for obtaining a strong adhesion. The layer thicknesses were validated by a profilometer, the total probe thickness was 15.6  $\mu\text{m}$ . In the future the

spinning speed of the first polyimide layer should be slightly increased to get an exact 7.5 $\mu\text{m}$  thick layer. Because unequal layer thicknesses might induce stresses that result in bent probes.

The lift-off process is a critical step with a substantial number of parameters to control. The mixed development solution was poured in a large bottle and can be considered as constant. An automated shaking system could be included to obtain more control over the development process. Even though the process was optimized, line failures remained. This might be due to contaminations, insufficient adhesion of the metal, lift-off problems or a combination of the former. In the current designs, the interconnection lines were designed parallel for the entire length of the probe shaft. Hence, further optimization could be undertaken: when the length of the probes can be shortened the number of line failures will decrease. Additionally, fanning out the lines along the probe shaft will simplify the lift-off process, at the expense of increasing the probe width, which is not desired.

The probe widths are dependent on the electrode surface area and pitch. The pitch can be decreased to sub micrometre level by using a quartz photomask or by e-beam photolithography instead of contact photolithography. Although, e-beam lithography is much slower than contact lithography. As another improvement, the electrode surface can be decreased without increasing the impedance by adding a layer of iridium oxide. However, this requires an extra photomask.

The probe outline and openings of the electrodes and connectors were made with RIE. RIE with only oxygen was more directive than expected, resulting in an electrode diameter narrower than the one targeted, which possesses a higher impedance. A high-directive etch process is beneficial because the designed pattern is almost identically etched. In a new mask design, the electrode opening diameter should be almost equal to the metallization diameter to optimize the electrode area and decrease the impedance. The probe width was slightly smaller than targeted, however this is not crucial.

In future probe designs, a compromise needs to be made between the electrode impedance, electrode diameter and probe width. When possible, the probe length should be decreased, this will reduce the chance of line failures. In addition, more probes can be accommodated on an equally sized wafer, hereby reducing the cost per probe. Additionally, to reduce the probe cost, glass carriers (e.g. soda lime glass) could be used instead of silicon carriers, and if possible, the carriers should be reused. These solutions can only be implemented if the probe quality is not affected.

Now that the flexible polyimide probes are produced, a delivery system is required for lowering an array of flexible probes into the target brain area without restricting the behaviour of the animal. This will be presented in the next chapter.

## Chapter 3: Hyperdrive, the probe positioning mechanism

*In this chapter the probe positioning mechanism will be discussed, which is further named hyperdrive. A 'hyperdrive' is formed by an array of microdrives, each 'microdrive' is a single lowering-drive unit [5, 38]. The previous two terms will be used throughout the thesis by the current definitions. When it is necessary to lower the probes gradually and independently into the brain tissue, a hyperdrive is indispensable. At first an overview will be given about the state-of-the-art hyperdrives. Hereafter a description of the design will be given, continuing with the fabrication process of the hyperdrive.*

### 3.1 State-of-the-art

Peroperatively inserting an array of probes, with a limited number of electrodes, to a targeted brain area is a laborious task [6]. Even if the targeted area would be reached the probes might drift off location, and herewith losing the ability to record from this area. A frequently applied solution is the use of a hyperdrive where the probes are gradually lowered over time with live feedback of the probe position from the electrophysiological signals [5, 39]. A hyperdrive enables simultaneous recordings of neurons within one brain area at different depths or across different brain areas [40]. Furthermore, a hyperdrive reduces the peroperative period, as the probes can be lowered to the exact target area post-operatively. Hyperdrives are essential tools for detecting and isolating extracellular single-unit activity in freely behaving rodents [39]. Adjustable electrodes are necessary to record from the 40  $\mu\text{m}$  thick pyramidal cell layer in the CA1 region, because the slightest movement of a probe after implantation makes it impossible to maintain stable unit recordings [38].

In general the main parts of a manually driven hyperdrive for recording brain signals in freely behaving animals are: 1) the main body containing an array of microdrives typically including micro-screws, 2) electrodes as described in chapter 2, and 3) an electronic interface board (EIB) for connecting the electrodes to the data acquisition system [41, 42], see figure 23.

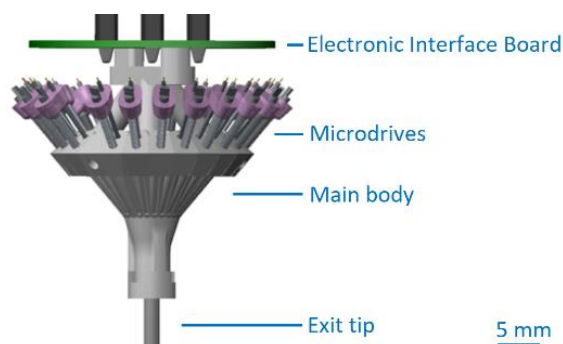


*Figure 23: Hyperdrive by Kloosterman et al. The hyperdrive has a cone-shape for implanting multiple electrodes into the brain. The hyperdrive is an assembly of the main body, microdrives with translating drive-screws, electronic interface board (EIB), and exit tip [8].*

Literature describes various hyperdrive designs, those are categorized as follows: 1) screw-driven shuttles with the screw fixed except for a rotation around its axis [6, 16, 20, 38, 43-54]. The shuttle converts rotary motion of the drive-screw into linear motion of the electrodes, 2) screw-driven with the screw rotating around its axis and translating within the fixed main body [7, 8, 55-61].

Another hyperdrive categorization is based on input motion. Input motion for lowering the electrodes can be: 1) manually driven and, 2) motorized driven, which is subdivided into: a) micromotors [6, 50-52, 54], b) piezoelectric actuators [39, 41], c) hydraulic [62] and d) MEMS-based hyperdrives [63]. All motorized designs are complex designs and won't be further discussed. This report focusses on manually driven hyperdrives.

Battaglia et al. and Headley et al. developed a hyperdrive with a rectilinear traversing of the electrodes, providing less friction when lowering the electrodes [16] [48]. When a specific position is targeted this comes at the cost that less electrodes can be positioned into the brain. A cone-shaped hyperdrive design is often used to expand the microdrive array and lower multiple electrodes into the brain tissue [5, 7, 8, 59, 64]. The electrodes meet in the bottom of the hyperdrive and slide through closely packed holes arranged in a grid, this is named the exit tip. Electrode guiding grids can be produced by drilling small holes close to each other forming an array [53, 65]. The benefit of using a guiding grid is that the position and pitch between the different electrodes is known [53]. A direct connection from the microdrives to the guiding holes is preferred as this reduces the assembly time.

The patented design by McNaughton comprises significant innovations for the manually driven hyperdrive design [7]. Namely, an increased array of independent adjustable electrodes, which are small and light-weight enough to allow freely behaviour of the rodent. By the increased array of electrodes, the number of laboratory animals is reduced without affecting the amount of research data [7]. Although it was later criticized by Stengel et al. that the hyperdrive of McNaughton is expensive and labour-intensive to assemble [66]. The patent of Stengel et al. states that manufacturing and assembly costs are significantly reduced by using less parts compared to McNaughton's design [66]. A commercialized version of Stengel's patent is the Neuralynx Harlan 28 drive [67]. In the last decade computer-aided design (CAD) and 3D-printing are often implemented for the fabrication of the hyperdrive parts [8, 20, 38]. Kloosterman et al. presented a hyperdrive that was designed and produced by these techniques, see figure 23. The design shares many features with the McNaughton patent [5, 8]. Both designs include a moving screw, which requires the double spacing within the hyperdrive. It is in terms of dimensions more beneficial to use the shuttle lowering design.

The electrodes are individually connected by gold pins to the EIB. Connecting an array of channels in this way is very labour-intensive. Further, the electrodes are freely hanging in the air, making the hyperdrive very fragile as breaking an 12  $\mu\text{m}$  electrode wire is easily done when manipulating a microdrive. In the design of Jeantet et al. the electrode wires are protected because the wires are inside the housing and lowered by a shuttle system that is driven by a set screw [68].

After surgery the rodent will try to release the implant by scratching or hitting the walls of their cage. To protect the hyperdrive from these accidents a protective cone and cap are necessary. Additionally the hyperdrive should be electrically shielded, meaning that a Faraday cage is required to block environmental noise and slow wave artefacts arising from the charged whiskers of the rodent [18]. Aluminium foil glued to a cone structure connected to the ground is often used for this purpose [38].

Assembling the hyperdrive of Kloosterman et al. is a labour-intensive process, it takes up to two weeks for an experienced scientist to assemble [8]. Therefore it is beneficial to retrieve the implant and recording electrodes after sacrificing the animal. This reduces the cost and assembly time. The hyperdrive of Kloosterman et al. measures 51.5 mm in height and  $\text{Ø}66.7$  mm in diameter and weighs 31.9 g. The weight of each microdrive is 173 mg with a custom drive-screw weighing 105 mg.

The goal of this thesis was the improvement of the manually driven hyperdrive to enable the insertion of the flexible polyimide probes into a freely behaving rat. The hyperdrive must enable stable unit recording of neurons for a long time period (weeks). This requires an implant that does not exceed the loading threshold of the animal's skull, which is approximately 10 percent of the rat's weight [50]. A Long Evans rat weighs between 300 and 600 g [48], this means the hyperdrive weight should not exceed 30 grams. Further the height of the hyperdrive without connectors may not exceed 5 cm [53]. Simultaneous the hyperdrive should be robust to extended experimental handling. Meaning that the electrodes and EIB are well protected and damaging the electrodes during manipulation is impossible. At last the hyperdrive should be reusable and simple to assemble.

This work proposes a new hyperdrive with 16 microdrives, that is small, re-usable, lightweight, easy-to-assemble and provides full protection of the probes and electronic interface board.

### 3.2 Design phase

The computer-aided design program SolidWorks<sup>19</sup> was used for designing the hyperdrive. The design includes 16 microdrives with the same outer dimensions as the state-of-the-art hyperdrive and ensures full protection of all its electronic components. With the new hyperdrive design 16 polyimide probes can be implanted into the rodent's brain, adding up to a total 256 recording sites. The design of the hyperdrive was improved over many iterations, see figure 24. A first design (A) contained 8 bulky microdrives and lacked an EIB holder and skull attachment structure. A later iteration (B) contained many improvements: 16 narrower microdrives, a skull attachment structure and EIB holder.

The final hyperdrive design (C) consists of: 16 microdrives with screw-driven shuttles, a 3D-printed main body that houses the microdrives, an exit tip to guide the probes into the brain, a structure to facilitate attachment of the hyperdrive to the skull, an electronic interface board, and an external shell and cap for protection. Each part is in detail discussed, followed by the fabrication processes and assembly.

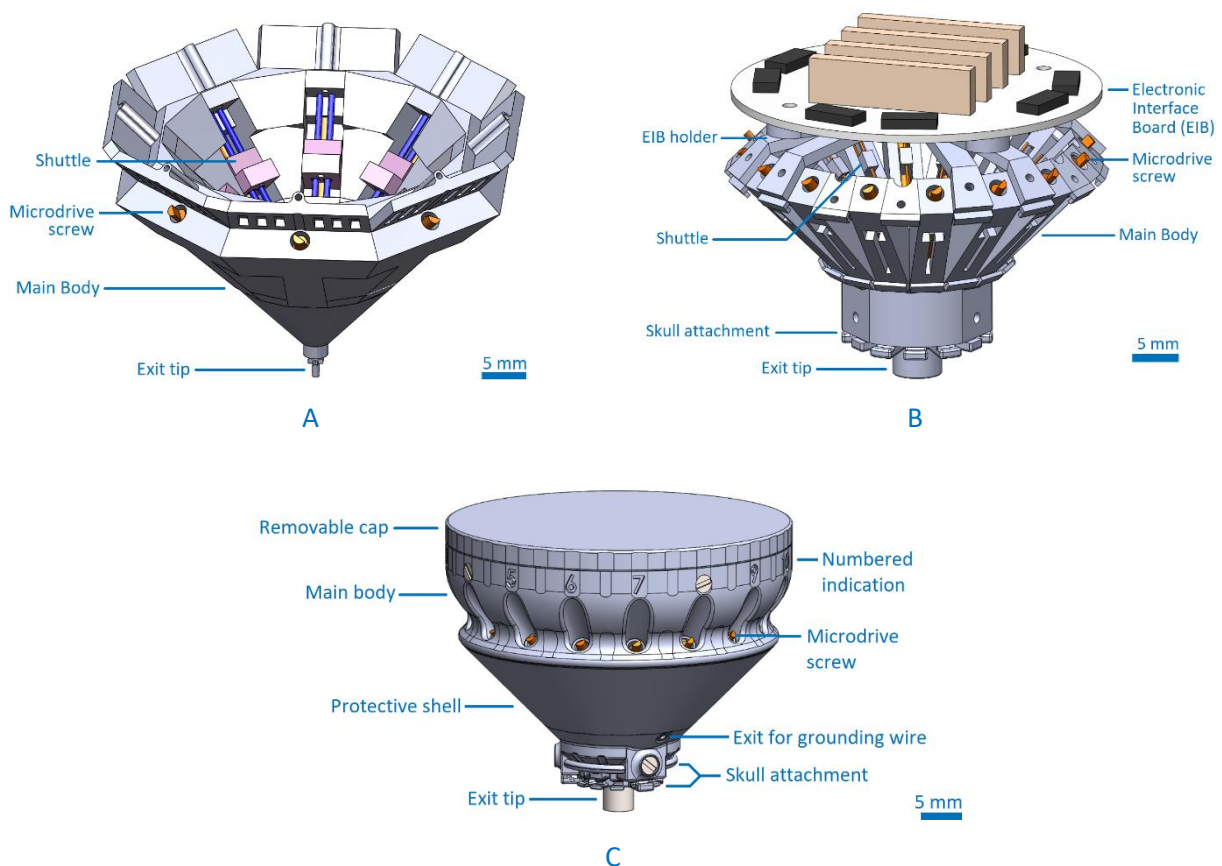


Figure 24: Hyperdrive chronology. A) The first hyperdrive design with 8 microdrives, B) A later iterative contained: 16 microdrives, a skull attachment and EIB holder. The EIB is shown on top, C) Final hyperdrive design, which is fully closed to protect the electronic components. The custom drive-screw heads are left open for manipulating the microdrives and the Omnetics connectors (under the removable cap) need to be accessible for connecting the headstages (figure 29B).

<sup>19</sup> Dassault Systèmes SOLIDWORKS Corp., Waltham, USA.

### 3.2.1 Microdrives: screw-driven shuttles

The main body is designed as an array of microdrives, arranged in a circle around the central axis. It was found from literature [16, 45, 48] that a shuttle lowering system requires less space than a screw lowering system, hence the hyperdrive design includes the shuttle system. Each microdrive contains: a 3D-printed body, custom-made drive-screw, shuttle, polyimide tubes, polyimide probe, and dental cement. By turning the screw the shuttle will drive the polyimide probe down into the brain. The custom screw head is fixated by dental cement, so its only degree of freedom is a rotation in the microdrive body. The 3D-printed body is designed conform to the shuttle and is necessary for guiding the shuttle downward without allowing rotation. The polyimide probe is inserted and glued in a polyimide tubing, which itself is glued to the shuttle.

To obtain a stable recording system four different types of screw-driven shuttle systems were tested, see figure 25. The major concern was the stability of the shuttle, but the weight was also taken into account.

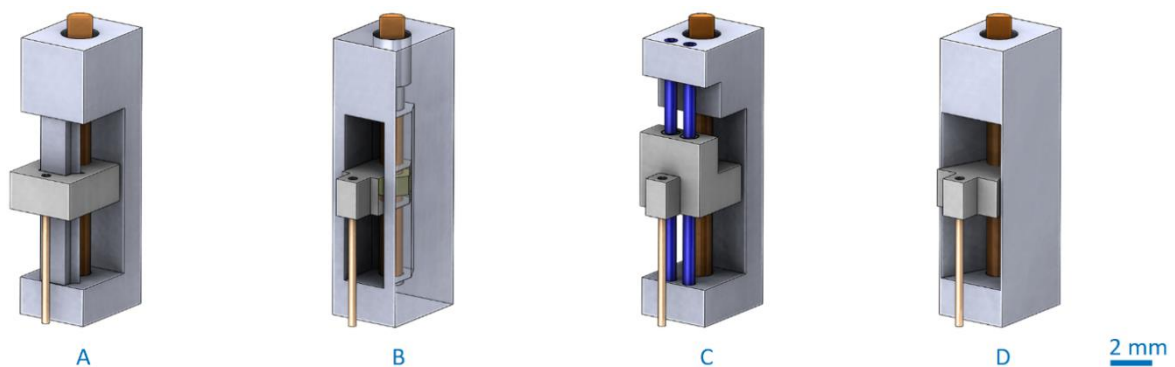


Figure 25: Four types of microdrives. All designs contain a body (grey), custom screw (orange), polyimide tube (pink) and shuttle (grey). A) uses an internal dove tail to support the shuttle. B) The microdrive is partly made transparent for clarity, the shuttle holds a brass nut (yellow) and is guided by the walls, C) uses gauges (blue) to support the shuttle, D) supports the shuttle by the side walls

Design A uses an internal dovetail to support the shuttle. In practice, a 3D-printed the shuttle and support with zero tolerance did not allow smooth movement. The weight is 328 mg. Design B contains a shuttle with 3D-printed nut holder and M1.2 brass nut, see figure 27. Manipulation of microdrive design B is almost frictionless due to the nut and the shuttle moves up and down without rotation. The weight is 419 mg with the nut weighing 54 mg. Design C contains four tubing's, two as guides (blue) and two shorter tubing's inside the 3D-printed shuttle to enable smooth movements. Although the movement was smooth, the shuttle could slightly rotate and therefore it was less stable than design B. The weight is 392 mg with the tubes weighing 25.2 mg (23 gauge) and 9.3 mg (20 gauge). Design D works similar as design B, but here the walls are slanted inwards and the shuttle was manually threaded. The weight is 382 mg. From the four designs it was found that the microdrive with the nut (design B) performed the best, backlash was insignificant and translation of the shuttle was very

smooth. Therefore this microdrive type was chosen to be incorporated into the array for the main hyperdrive body.

The custom made screw was previously used in the design of Kloosterman et al. [8] and features a M1.2x0.25 threaded part, halfmoon screwhead, and a smoothed part with flange that will be enclosed by dental cement to allow rotation and prevent translation of the screw.



Figure 26: Custom made microdrive screw adapted from Kloosterman et al. [8]. 3D-view of the hyperdrive screw and side view.

The fabrication process of the custom screws is a sequence of turning and milling operations and will not be discussed in detail.

The shuttles are comparable to a nut with an extension and are used to lower the probes into rodent's brain. The initial design of the shuttles consisted of a brass nut that was clamped into a SLA 3D-printed holder, see figure 27A. The shuttles are designed as an assembly because threading in polymer parts is not durable. The assembly is also the disadvantage of this design as it allows a rotation of the nut within the plastic holder when the torque exceeds the clamping threshold. This makes the microdrive unusable and hence, the probe depth cannot be adapted. Therefore a single piece shuttle was designed, see figure 27B. The production process of this stainless steel shuttle is discussed in detail at the fabrication section.



Figure 27: Custom designed shuttles. A) 3D-printed shuttle with nut holder (grey), M1.2 nut (yellow). The arrow indicates the assembly of the nut and its holder. B) Stainless steel shuttle, the height is halved compared to the assembled version, increasing the travel length by 1 mm.

To protect all electronic equipment a wall was built on top of the hyperdrive, including supportive structures for fixing the EIB. The inside of the protective wall is foreseen of overhangs, so that the probes can hang underneath these structures. Numbers are engraved on the outside of the protective wall for easy indication. Finally all edges are smoothed.

### 3.2.2 Polyimide tubes and exit tip

Polyimide tubes<sup>20</sup> are necessary for guiding and stiffening the flexible probes within the hyperdrive. Two sizes are used: 1) outer tubing that guides the probe from the microdrive to the bottom of the exit tip, 2) an inner tubing that is glued to the shuttle and slides through the outer tubing. The polyimide probes are inserted through the inner tubing.

The benefit of an exit tip is that there is no need to route all the tubes manually as the bottom pattern is predefined. Two different exit tip designs were made, see figure 28. In design A the polyimide tubes are inserted until a transition to rectangular slots which run to the bottom of the exit tips. The rectangular slot size is 100x200  $\mu\text{m}$ , which enables a tight guiding for the flexible probes. In design B the outer polyimide tubes are inserted through the whole exit tip, glued at the bottom and cut orthogonally. The conduits ensure a rectilinear travelling of the probes. The conduit pattern can be adapted to the needs of the neuroscientist. In this thesis it was chosen to have a central probe with the other probes densely packed around it at an equal centre-to-centre distance.

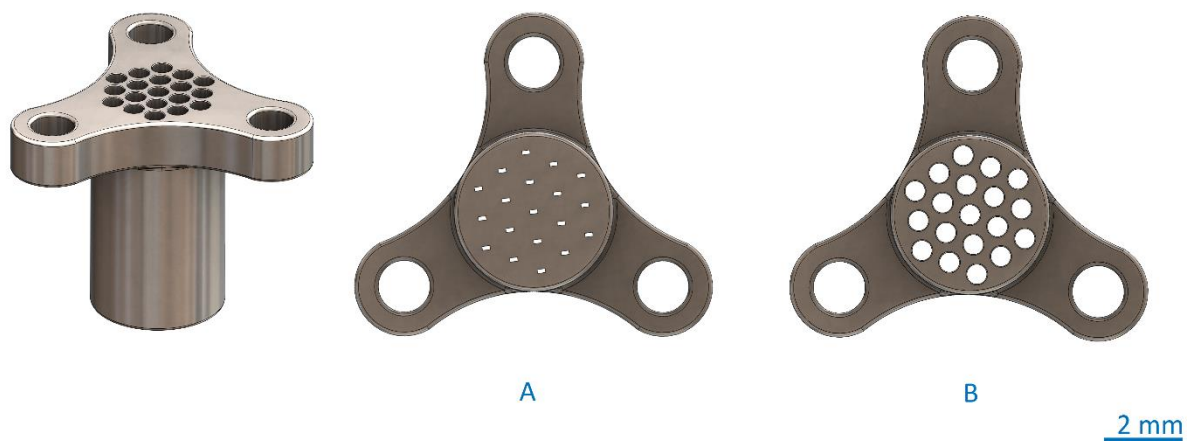


Figure 28: Two exit tip designs. A) Rectangular slots type allows very precise guiding of the probes. B) Round conduit type.

<sup>20</sup> Nordson Corporation, Westlake, Ohio, United States.

### 3.2.3 Skull attachment structure

The skull attachment structure is a crucial part of the brain implant because it forms the interconnection from the hyperdrive to the rodent's skull. The shape of the skull attachment structure is minimal but still robust to ensure the rigid connection with the skull. Bone screws<sup>21</sup> are fixated into the rodent's skull and a wall of dental cement is built between the screws. The hyperdrive is positioned above the dental cement wall and fixated by the addition of more dental cement, which encapsulates the flanges of the skull attachment structure providing a rigid fixture. For more details about the surgical procedure, see section 4.3.1.

### 3.2.4 Electronic interface board with zero-insertion-force connectors

The existing electronic interface board<sup>22</sup> (EIB) with eight zero-insertion-force<sup>23</sup> (ZIF) connectors enables a seamless connection for the flexible polyimide probes. In this way an array of 16 electrodes is attached to the EIB in one go. The connecting part on the flexible polyimide probes is conform to the ZIF-connector, see chapter 2. Two ZIF-connectors are routed to one Omnetics<sup>24</sup> connector that consists of 32 electrode channels. Four Omnetics connectors are implemented on the EIB enabling simultaneous recording with 128 electrode channels. During an experiment headstages are attached to the Omnetics connectors to pre-amplify the electrophysiological signals which are then transferred to the data acquisition system<sup>25</sup>.

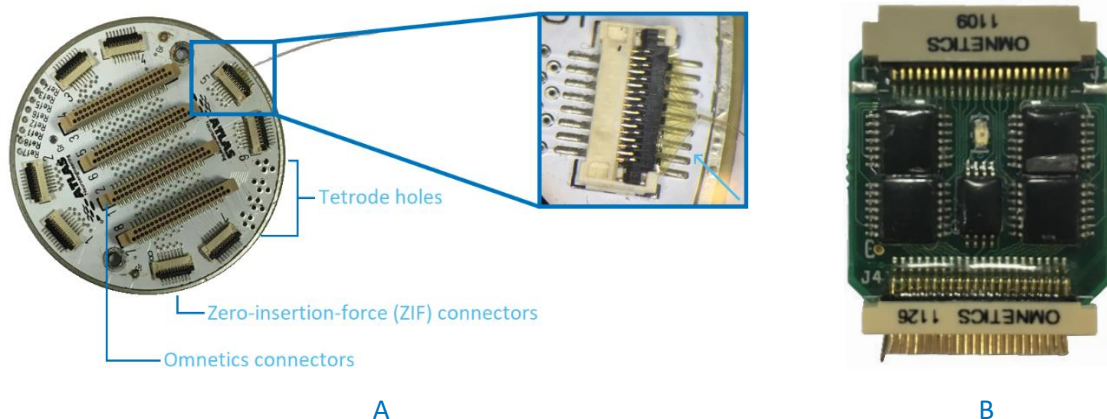


Figure 29: Electronic Interface Board (EIB) and Headstage. A) The EIB contains 4x tetrode connection holes, 4x Omnetics connectors and 8x zero-insertion-force connectors (ZIF). The ZIF connectors are used to connect the flexible probes (magnification, arrow). B) Headstage for pre-amplification is connected to the Omnetics connectors, hereafter the signals are send to the data acquisition system.

<sup>21</sup> 19010-00, Fine Science Tools, Germany

<sup>22</sup> EIB 128Ch, Atlas Neuroengineering, Leuven, Belgium

<sup>23</sup> Molex, Lisle, Illinois (subsidiary of Koch Industries)

<sup>24</sup> Omnetics 1148, Omnetics Connector Corporation, Minneapolis, Minnesota, United States

<sup>25</sup> Digital Lynx SX, Neuralynx, Bozeman, Montana, United States

### 3.2.5 External shell and protective caps

The protective cone is directly connected to the skull attachment reducing the number of assembly steps. The cone provides protection to the microdrives and prevents the intrusion of dust. In addition, a conductive graphite coating<sup>26</sup> is applied forming a Faraday cage that shields the brain implant from noise, e.g. 50 Hz-line noise.

A permanent cap is screw fixed on top of the hyperdrive, closing the whole system except for the Omnetics connectors and the head of the custom drive-screws. This allows easy and secure manipulation of the microdrives while handling the animal or lowering the probes. When the rodent is at rest in its cage, the top of the hyperdrive is closed by a protective cap, which is easily attached and detached by a magnetic connection. Four small Neodymium ring magnets<sup>27</sup> are glued to the protective cap and four washers are inserted into the permanent cap. It was chosen to put the magnets into the removable cap so that there is no distortion of the electrical signals during recording.

---

<sup>26</sup> Graphit 33, Kontakt Chemie, Iffezheim, Germany

<sup>27</sup> Supermagnete, Gottmadingen, Germany

### 3.3 Fabrication processes

#### 3.3.1 3D-printed parts

The complex shapes of the main body, permanent cap, removable cap and skull attachment structure were 3D-printed by stereolithography (SLA) which is a vat photopolymerization technique. The reason to choose stereolithography over other printing techniques is that the surface quality is outstanding.

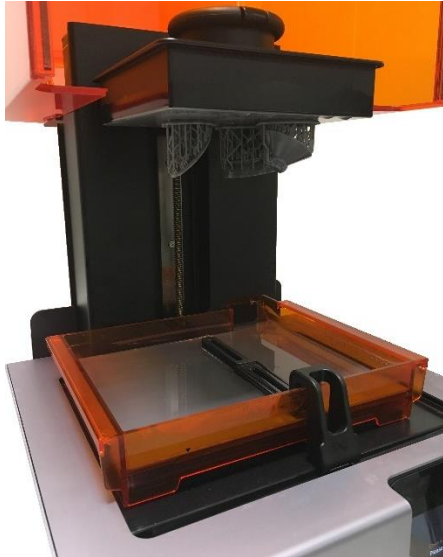


*Figure 30: Formlabs Form 2 3D-printer. At the bottom: the resin tank including the sweeper (black), and at the top: the hyperdrive parts (grey) attached to the building platform (black) after 3D-printing. The cover (orange) is closed when the 3D-printer is operating.*

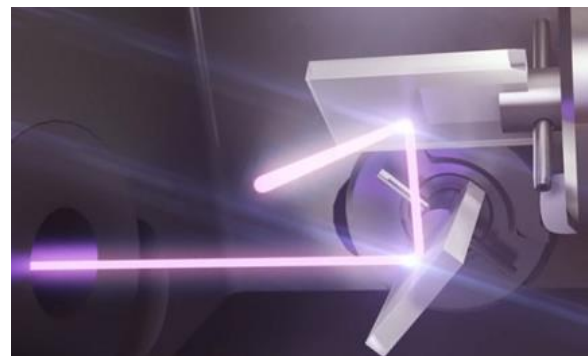


*Figure 31: Inside Formlabs Form 2 3D-printer [69]. Mirror galvanometers along the x- and y-axis are used for rapidly aiming the laser beam across the resin tank.*

The Formlabs Form 2, see Figure 30, is a bottom-up 3D-printer that operates with a photopolymerizable resin which is cured by a point laser [69, 70]. The building platform is lowered in the z-direction in proximity of the resin vat and the laser cures the liquid polymer at specified design positions. Mirror galvanometers along the x- and y-axis are used for rapidly aiming the laser beam across the resin tank, hence curing and solidifying the resin, see figure 31 [70].

The building platform is separated from the base of the vat by slide peeling which generates the lowest separation force enabling printing of large parts [69]. If the separation stresses are too high the cured layer may adhere to the vat base instead of the building platform resulting in part failure. It is also important to work with a clean building platform as the first layer is the most critical and must adhere well to the building platform. SLA printed parts are usually built inclined to further reduce the peeling forces. After separation, a sweeper is moved within the vat to ensure a uniform coverage of uncured resin for the subsequent curing step. The building platform is lowered and the entire process is repeated, curing the resin layer-by-layer until the whole part is formed. The base of the resin tank features a special coating, usually polydimethylsiloxaan (PDMS) or fluorinated ethylene propylene

(FEP), to prevent sticking of the photoresin to the vat and assisting with the separation [70]. Therefore, it is important to replace the resin tank regularly to maintain optimal printing conditions [70].

In bottom-up vat photopolymerization it is recommended to print at an angle to reduce separation forces. Herewith the support structures are increased, but this is not the primary concern. The support structures are always of the same material as there is only one photoresin vat, requiring manual removal. Printing the support structures as small as possible and with the lowest density will minimize the influence on surface quality.

The parameters to be set by the operator are: material choice, layer height, part orientation and support structure locations. The layer height can be set on 25, 50 or 100  $\mu\text{m}$  and for the hyperdrive parts it was set to 25  $\mu\text{m}$ . The surface finish and accuracy of the part is determined by the layer height and light source resolution or spot size [70], which is 140 micron for the Formlabs Form 2 3D-printer [69]. SLA can cure different photoresins, those determine the layer height. The standard Formlabs resins were preferred as a layer height of 25  $\mu\text{m}$  could be applied.

After 3D-printing, there are two post-processing steps. First, an automated washing<sup>28</sup> step took place for 10 min in isopropyl alcohol (IPA), a stirrer ensures that every corner and hole is thoroughly cleaned. After washing the IPA is evaporated for 30 min and the parts were release from the building platform. Second, the models were placed into a post-curing machine<sup>29</sup>, which will maximize the mechanical properties of the SLA printed parts. Post-curing is done for 30 min at 60 °C with 405 nm LEDs, the optimal wavelength for curing photoresins, and is necessary for optimizing the properties of the 3D-printed parts [70]. Subsequently the support structures are cut to release the parts from the base. Sanding and polishing are usually not necessary if the appropriate support size and density is chosen.

### 3.3.2 Laser-cut stainless steel shuttles

The shuttles were laser-cut from a 1 mm thick stainless steel plate, deburred, pre-drilled with a 0.9 mm drill bit and manually threaded with a M1.2 threading tap.

Laser-cutting is a thermal separation process which can cut a variety of materials by moving a focused laser beam along the surface of a workpiece [71]. A laser (light amplification by stimulated emission of radiation) is a coherent, monochromatic and collimated bundle of light that can be focussed on a tight spot [72]. The beam is generated by a laser resonator and bend in different directions by mirrors, or beam-benders, before it is focused by the lens within the laser cutting head. Focusing the laser beam to a concentrated spot raises the power density above  $10^6 \text{ W/cm}^2$ , where most metals reach a liquid or vapor state [72]. The power density is extreme when compared to the output of sunlight in the

---

<sup>28</sup> Form Wash, Formlabs, Somerville, Massachusetts, United States

<sup>29</sup> Form Cure, Formlabs, Somerville, Massachusetts, United States

atmosphere, which is less than  $0.1 \text{ W/cm}^2$  [72]. The focused laser beam travels together with a pressurized gas flow through a nozzle before hitting the workpiece. Stainless steel is simply molten by the laser beam and effortlessly removed from the kerf by a pressurized gas flow. The assist-gas also shields the heated material from the surrounding air, resulting in oxide free cutting edges [71].

Mainly two types of laser resonators are used: 1)  $\text{CO}_2$  laser, 2) neodymium: yttrium-aluminum garnet (Nd:YAG) laser<sup>30</sup>. Both lasers emit light with a wavelength in the infrared light spectrum, which are invisible to the human eye. Motor drives with a computer-numerical control (CNC) system are used to direct the laser cutting head in the shape of the design pattern. The height of the focal point affects the cut quality and can be set just above the surface, within the surface, or underneath the surface.

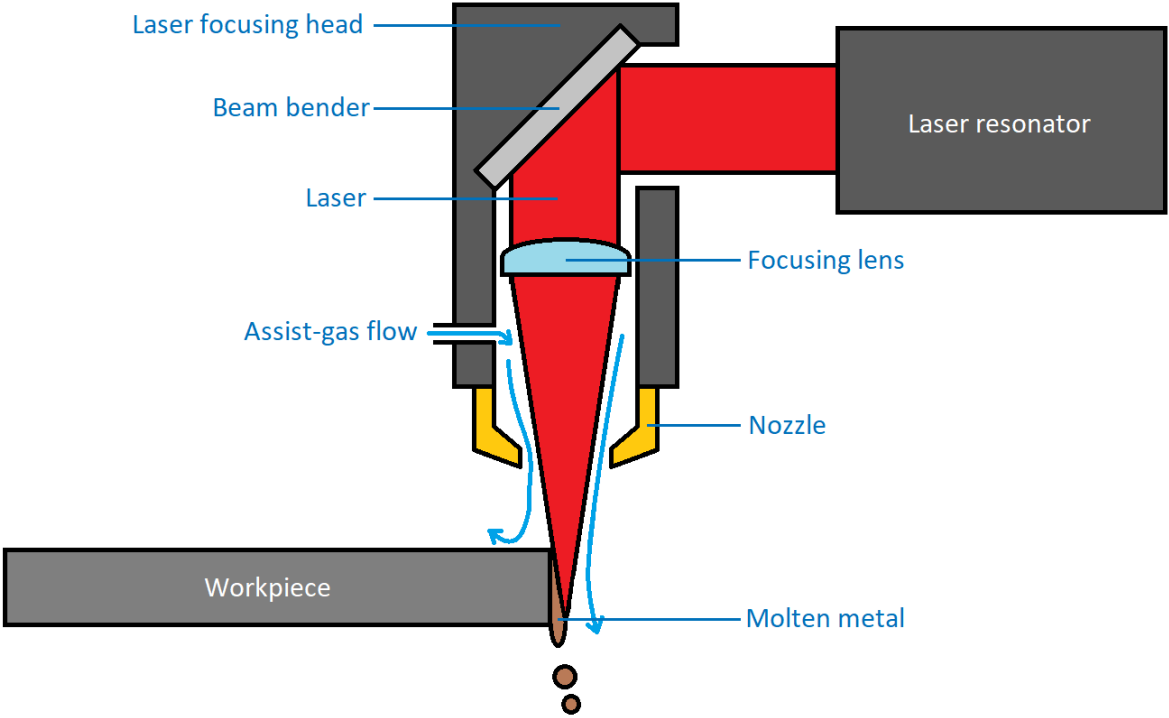
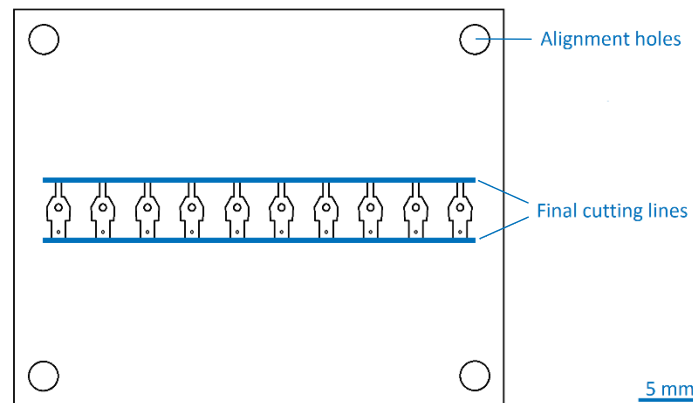


Figure 32: Basic principle of a laser cutter. The laser resonator generates the laser beam, which is bend by a mirror continuing its path through a lens that focusses the laser to a tight spot. Due to the extreme power density metals like stainless steel are simply molten. Figure adapted from [73].

<sup>30</sup> JK Laser/SDI lasers, Southampton, United Kingdom

First the shuttle outline and holes were laser cut with a 1064 nm Nd:YAG-laser, see figure 33. This is done simultaneously as the holes need to be exactly centred within the outline. Four holes were cut in the corners to align the workpiece for the second cutting step.



*Figure 33: Drawing of the cutting pattern for 10 microdrive shuttles. The shuttle outlines, holes and alignment holes (black) were cut first. The thick lines (blue) were cut at the final step to release the shuttles from the base material.*

Hereafter the workpieces were dipped in buffered HF and immersed for 3 hours in 3:1 HNO<sub>3</sub> solution in combination with an ultrasonic cleaner for deburring. The stainless steel workpieces were placed into a specially fabricated holder, figure 34, to maintain well alignment and proper guidance of the drill bit and threading tap. The polymethylmethacrylate (PMMA) holder part was cut with a CO<sub>2</sub>-laser.



*Figure 34: Prototype of the final holder. The holder features guiding holes for the drill bit and threading tap to precisely align with the cut holes.*

After threading the pieces were released from the stainless steel base plate by laser-cutting the top and bottom, see thick blue lines in figure 33. The holes were drilled and tapped manually which takes some time but the benefit is that the shuttles cannot rotate and can only travel up and down. Other advantages of the stainless steel shuttle are: improved reusability compared to the shuttle nut holder design and a 1 mm gain in travel length, hence, the total travel length is 8 mm.

For a large batch of shuttles the production process should be outsourced to a company that is capable of laser-cutting and computer numerical controlled (CNC) milling with automated tapping.

### 3.3.3 Direct metal laser sintering of the exit tip

Four manufacturing techniques were considered for the fabrication of the exit tip: (1) computer numerical controlled (CNC) milling, (2) etching, (3) moulding, and (4) 3D-printing.

(1) Computer numerical controlled (CNC) milling is a subtractive process that uses milling and drilling tools to remove material. The small cannula dimensions of the first design do not allow a milling tool to remove the material, the second design would be feasible to fabricate on a CNC mill. Although the holes need to be drilled in a pulsed manner because drilling instantly will break the drill bit. On prediction five hours are required to mill a single exit tip from aluminium. Hence, CNC-milling is not the preferred fabrication method for the exit tip. CNC-milling is a single piece production process which will take a lot of time when more parts are needed.

(2) Etching is a subtractive process that uses acids to remove material. Etching restricts the part size to the maximum wafer thickness, which is typically 525  $\mu\text{m}$  for a 4 inch wafer. A part of a few millimetres thick becomes challenging and can be realized by two methods. First, several wafers can be bonded together by fusion bonding. This requires 10 wafers for a 5 mm long part. Second, thicker wafers can be used but this solution requires a very directive etching process. Both the thick wafer and production process make etching process expensive. The part dimensions should be reconsidered to apply etching as the fabrication technique. This means that the conduit length must be shorter.

(3) Moulding is a formative process that uses a model negative of the object which is filled with a fluidic material. For the mould production very small stiff strips or pillars of material are required that will serve as the negatives for the conduits. For a single hole mould production could be feasible. However, mould production becomes complex when arranging the holes in a pattern. Therefore moulding is not further considered as a production method for the exit tip.

(4) 3D-printing is a preferred solution because complex shapes can be easily formed. Unfortunately, the current 3D-printers are not accurate enough to print the rectangular slot sizes, certainly not if the part should be made of a metal. Two specialized 3D-printing companies were contacted for the fabrication of the rectangular slot design, however, it was never actually tried because of the uncertainties. The additive manufacturing department of KU Leuven did not succeed neither in printing the small rectangular slots. A possible solution for 3D-printing the slots could be two photon polymerization (2PP), which is capable of printing micrometre scale features by ultrashort laser pulses in a polymerizable photosensitive resin. Although 2PP is not capable of printing the outer dimensions.

The second design was 3D-printed with the previous discussed SLA technique. Tests were executed with the biocompatible dental SG resin of Formlabs, the layer height for this material is restricted to 50 microns, which is too inaccurate for 3D-printing the holes. The part could be 3D-printed with the

stand resins with a layer height setting of 25 micron. Unfortunately the standard resins are not biocompatible and a polymer is less reusable than a metal. Stainless steel and titanium were considered as potential materials.

Direct metal laser sintering<sup>31</sup> (DMLS) was the applied method for producing the second design from the titanium alloy Ti-6Al-4V. Titanium was chosen for its biocompatible properties and reusability. Direct metal laser sintering (DMLS) is a variant of powder bed fusion, that uses a thermal source to induce fusion between metal particles layer-by-layer [70]. The accuracy and surface quality of DMLS relies on the laser spot size, layer height and powder geometry. DMLS is capable of fusing metal alloys together on a molecular level without melting the powder. Full melt fusion would only be possible for a single element material, this technique is called selective laser melting (SLM). Due to the high processing temperatures the parts may warp due to residual stress, making support structures essential for limiting the probability of any deformation that might occur. In addition, the support structures act as a heat sink for the thermal generated energy. Annealing of the parts, while still attached to the building platform, is common for releasing residual stresses [70]. After annealing the parts were released from the building platform by wire electrical discharge machining (EDM). For a smooth outer surface it is recommended to tumble the parts.

### 3.4 Assembly of the hyperdrive

The different 3D-printed parts are connected by screws for reusability and simple accessibility. M1.2 threaded inserts are pressed into the holes of the main body and fixed with glue<sup>32</sup>. The exit tip is fixated by three screws to the main body and the outer polyimide tubes are inserted into the guidance holes of the exit tip. The outer polyimide tubes are glued at the bottom of the exit tip as well as to the main body. Next the shuttles are installed together with the custom screws. The screws are fixated around the flange with dental cement. The inner polyimide tubes are inserted through the shuttles hole and next through the outer polyimide tubes until the bottom of the exit tip. The inner polyimide tubes are glued to the shuttles and cut at the bottom of the exit tip with the shuttles fully lowered. The probes are inserted through the inner polyimide tubes until the bottom of the exit tip and glued to the inner polyimide tubes with the shuttles fully retracted. The probe configuration within the hyperdrive is found in appendix E. The cover is coated with graphite spray and fixed to the hyperdrive by three screws. A grounding wire is attached from the cover to the EIB. Another grounding wire is connected from the EIB to the outside. The EIB is fixed to the main body by two screws. The probes are connected to the EIB by the ZIF connectors and are held underneath the overhangs in the protective wall. The

---

<sup>31</sup> Concept Laser, General Electric Additive Manufacturing, Lichtenfels, Germany

<sup>32</sup> Cyanoacrylate, R&G Faserverbundwerkstoffe GmbH, Waldenbuch, Germany

system is closed by the permanent cap which is screwed to the protective wall. Finally, the removable cap is placed over the permanent cap.

### 3.5 Results

The final hyperdrive is an assembly of specialized parts. The impedance of the graphite coating on the protective cone was approximately 1.5k $\Omega$ . The diameter of the hyperdrive is 45 mm and the total height is 38.4 mm. The weight of the hyperdrive is 24,9 g. Weights of the individual parts can be found in appendix C.



*Figure 35: Final version of the hyperdrive. It contains 16 microdrives indicated by numbers. The probes are lowered through the exit tip by turning the microdrive screws. The graphite coating creates a Faraday cage around the electric components. The Omnetics connectors send the recorded signals to the outside. The skull attachment flanges are used to connect the device to the rodent's skull. The removable cap with magnets is not shown.*

### 3.6 Discussion

A new hyperdrive with 16 shuttle lowering microdrives was developed. Each microdrive contains: a custom screw, stainless steel shuttle, housing, polyimide tubes and flexible polyimide probe. The new hyperdrive height is 38.4 mm and diameter is 45 mm. The dimensions are considerably decreased in comparison with the previous design used at NERF, respectively 51.5 mm and  $\varnothing 66.7$  mm. The hyperdrive is mechanically protected by a cone and electrically shielded by a graphite coating forming a Faraday cage. The impedance is approximately 1.5k $\Omega$  and cannot be further decreased by graphite spray. If a lower impedance is necessary, conductive nickel spray<sup>33</sup> or a layer of evaporated aluminium could be applied. Nonetheless, those solutions are more expensive than applying a graphite coating.

The 3D-printed parts are assembled with M1.2 screws and threaded inserts. Ideally the threaded inserts are installed by a heated installation tip, which will melt the part, forming a strong connection around the knurls of the threaded insert. This technique is feasible with thermoplastics used in fused deposition modelling (FDM), but not with photopolymer SLA parts because the material deflects when heated. Therefore, the threaded inserts were glued into the printed parts. The assembly time is approximately one day, this is a major improvement compared to the previous design where it required two weeks. Further simplifying the assembly could be done by 3D-printing the tubes that connect the microdrives to the exit tip, by fanning out the tubes like a bouquet of flowers, see figure 36. The present exit tip holes are round and if a tighter guiding is necessary another production method for the slotted exit tip should be found. In 3D-printing the minimum hole size depends on the diameter and length of the conduit. Therefore, it could help to decrease the exit tip height, so that 3D-printing the slots becomes feasible. Another advantage of the slots is that less biofluid can enter the conduits, so micromanipulation remains smooth. This can also be achieved by making the exit tip surface hydrophobic, e.g. by etching pillar-like structures [74]. If different brain areas are targeted, the hyperdrive design can be easily modified to include two separate exit tips.



Figure 36: Proposed exit tip design for easier insertion of polyimide tubes.

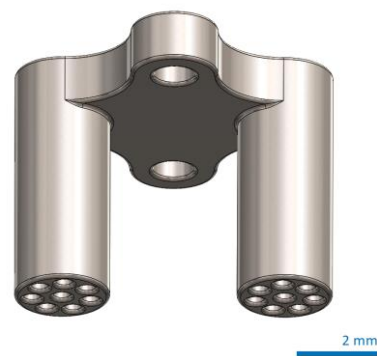
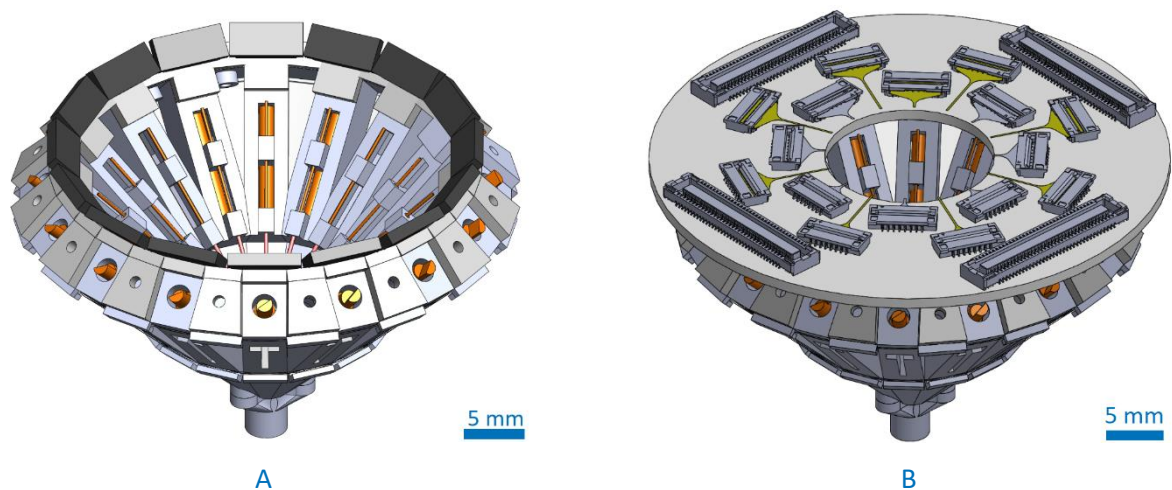


Figure 37: Proposal for a dual exit tip for targeting at least two different brain areas

<sup>33</sup> Electrically conductive nickel coating 3801 Holland Shielding systems

The electronic interface board (EIB) is necessary for bundling and transferring the electrode signals to the data acquisition system. The current EIB can accommodate 128 electrodes, however the new hyperdrive design can hold up to 256 recording sites. In the future the aim is to implant even more electrodes for enabling more simultaneous recordings. The new EIB should at least hold 16 flexible probes with a simple attachment like the zero-insertion-force (ZIF)-connector.

Two new EIB designs are proposed for connecting 256 recording channels, see figure 38. Design A uses a flexible EIB with an array of ZIF connectors for the probes. The flexible EIB would be connected to a rigid EIB on top by Molex connectors, not shown in the figure. The second design uses two rigid EIBs, the bottom EIB is shown in the figure and contains 16 ZIF connectors. The probes are connected through an opening in the bottom EIB. The bottom EIB would be connected by Molex connectors, to a top EIB, not shown in the figure.



*Figure 38: Proposed EIB designs. A) Flexible EIB containing 16 ZIF connectors (black). The flexible EIB will be connected to a rigid EIB for pre-amplification, which is not shown here. B) Rigid EIB with central hole for pulling the probes (yellow) through. The probes are connected to the ZIF connectors. The EIB would be connected to a top EIB for pre-amplification and data acquisition, not shown in the figure.*

The stacked EIB structures help to scale up the number of probes without increasing the diameter of the hyperdrive, although the height will slightly increase when stacking layers. The rigid EIB design is easier to produce than the more challenging flexible EIB. The flexible EIB has the benefit that the probes remain within the main body, herewith the diameter and height is maintained or slightly decreased. In the past it was proven that flexible EIBs reduce the total weight of the hyperdrive [16, 39]. Additionally, the probe length can be shortened as the ZIF-connectors are in close relation to the shuttles. This is advantageous because more probes can be accommodated on a single wafer and the chance on line failures becomes less.

The Omnetics connectors on the EIB could be replaced with magnetic connectors for a smoother connection when manipulating the animal. An example is the Neuralynx Quickclip® system.

Signal processing chips can be incorporated within the EIB to improve the signal quality. Nevertheless, it should be noticed that chips produce heat that should be properly drained. To enable more advanced navigation experiments in a three dimensional maze, a wireless connection from and to the data acquisition system should be implemented.

If a more precise manipulation of the microdrives is required a motorized design should be considered. Yang et al. stated that manually driven hyperdrives often increase the likelihood of drifting the electrode when lowering [39]. Another drawback of manual hyperdrives is that the level of behavioural stress might increase because the animal resists restraint during manipulation of the electrodes [39, 41], this makes single-unit isolation difficult [50]. The controllability and repeatability of manual hyperdrives are inferior compared to the motorized hyperdrives used for acute experiments [6, 50]. A manually driven hyperdrive is restricted to the user's ability to move the screw accurately and can never be as precise as with a motorized drive, which can reach increments of 2  $\mu\text{m}$  [6, 39]. Systematic cluster changes were not observed with such small increments, so steps of 8  $\mu\text{m}$  appeared to be sufficient [51, 52].

The benefit of using a piezoelectric actuator is that there is no need to transfer from rotative to linear motion and the positioning is much more precise [39, 63]. The cost of a piezoelectric actuator is also much lower than that of a conventional motor in this size range [39]. Although of all the benefits of motorized hyperdrives, only a limited number of electrodes can be lowered into the brain [39]. One exception is the hyperdrive design of Yamamoto et al. where 21 microdrives can be independently advanced without an excessive weight (29 g), however, the size of the hyperdrive was  $\pm 40$  mm wide and  $\pm 60$  mm high [51, 52]. One should keep in mind that this hyperdrive uses very expensive motors for manipulating the electrodes, the cost of one Faulhaber 1.9 mm motor, including the controller and gear head, is \$1000,- [6].

## Chapter 4: Validation of the brain implant

*This chapter describes the validation of the brain implant: flexible probes and hyperdrive. Two in-vitro tests were performed: 1) an insertion test in 0.6% agarose gel for simulating the brain tissue, and 2) an impedance test to check recordability. Finally the system was tested in-vivo in a rodent's brain.*

### 4.1 Insertion test

To validate the penetration ability of the flexible polyimide probes an insertion test was performed in agarose 0.6%. Agarose gel at a concentration 0.6% closely resembles the rodent's brain [21]. The agarose gel was made by microwave heating a suspension of agarose powder<sup>34</sup> and high purity water. The content was poured in a petri dish and close with a 3D-printed cap. The cap contains several holes and was designed to mimic the brain craniotomy. The exit tip was installed into a hole and the probe was gradually lowered by a microdrive into the agarose gel, see figure 39.

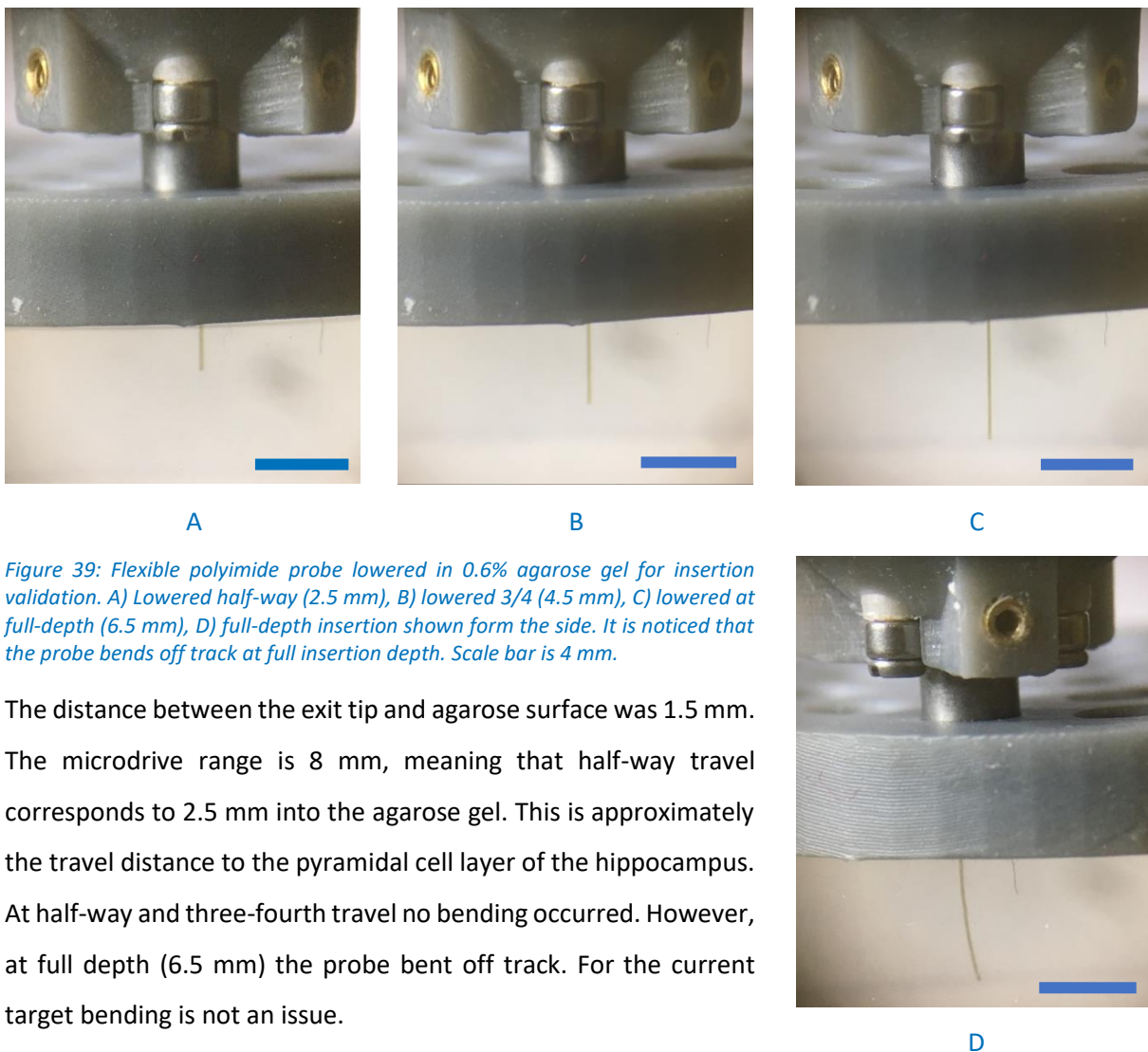


*Figure 39: Flexible polyimide probe lowered in 0.6% agarose gel for insertion validation. A) Lowered half-way (2.5 mm), B) lowered 3/4 (4.5 mm), C) lowered at full-depth (6.5 mm), D) full-depth insertion shown from the side. It is noticed that the probe bends off track at full insertion depth. Scale bar is 4 mm.*

The distance between the exit tip and agarose surface was 1.5 mm. The microdrive range is 8 mm, meaning that half-way travel corresponds to 2.5 mm into the agarose gel. This is approximately the travel distance to the pyramidal cell layer of the hippocampus. At half-way and three-fourth travel no bending occurred. However, at full depth (6.5 mm) the probe bent off track. For the current target bending is not an issue.

<sup>34</sup> Life Science Agarose I, VWR, Radnor, Pennsylvania, United States

## 4.2 Electrical test

The electrical impedance of the individual electrodes was validated in saline NaCl 0.9%, a solution that mimics the osmotic value of soft tissue. The probes were connected to the ZIF-connectors and individually lowered into the solution. The channel mapping of the probes to the NanoZ interface can be found in appendix D. In total 4 out of 9 of the 2x8 probes had over 10 working channels. For example, a 2x8 probe with 13 working electrodes had an initial mean value of 3.335 M $\Omega$  with a sample standard deviation of 1.172 M $\Omega$ . The three other channels showed impedance values above 10 M $\Omega$  and were considered as disconnected. Electrodes with impedance values in the M $\Omega$ -range are not able to record electrophysiological signals. Therefore, the electrodes were gold plated in order to decrease the initial impedances values<sup>35</sup>. The plating sequence is shown in table 3. Each run yielded a 1 s interval with an intermediate pause of 1 s, with the current applied at a frequency of 1004 Hz.

*Table 3: Gold plating sequence. Three steps are executed to lower the impedance sufficiently.*

Gold plating steps	1	2	3
Current [ $\mu$ A]	- 0.150	-0.05	-0.025
Target [k $\Omega$ ]	500	400	300
Runs	10	10	10

The impedances of the 2x8 probe after gold plating are shown in table 4.

*Table 4: Impedance values of the electrodes of a 2x8 probe. Gold plating (step 1-3) reduces the electrode impedance significantly, see figure 40. The red values indicate disconnected electrodes, the green values show targeted impedance values ( $\leq 300$  k $\Omega$ ).*

Electrode #	Initial magnitude (M $\Omega$ )	Step 1 (M $\Omega$ )	Step 2 (M $\Omega$ )	Step 3 (M $\Omega$ )
1	4.083	1.195	0.374	0.294
2	4.466	1.248	0.37	0.289
3	1.431	0.454	0.356	0.291
4	4.771	0.641	0.389	0.294
5	1.474	0.364	0.335	0.287
6	4.083	0.849	0.381	0.292
7	1.437	0.514	0.35	0.298
8	4.000	0.719	0.865	0.289
9	3.693	0.718	0.368	0.295
10	3.986	0.838	0.366	0.291
11	3.330	1.743	0.399	0.296
12	3.711	1.295	0.377	0.298
13	24.474	23.302	23.454	24.303
14	30.805	27.949	27.494	29.469
15	32.411	30.853	32.757	30.773
16	2.894	1.581	0.382	0.294

<sup>35</sup> Neuralynx, Bozeman, Montana, United States

The difference between before and after gold plating is visualized by a bar chart, see figure 40.

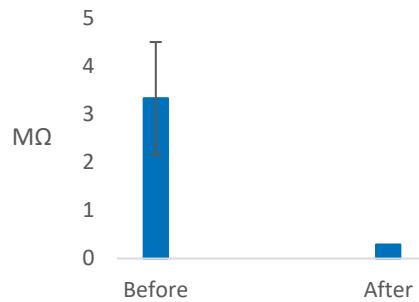


*Figure 40: Mean impedance values before and after gold plating for the 2x8 probe. Gold plating reduces the electrode impedance significantly. The bars present mean impedance values and standard deviation (n = 13 electrodes).*

The mean value after gold plating was 293k $\Omega$  with a sample standard deviation of 3.45 k $\Omega$ . The impedance values of all the probes inserted in the hyperdrive are found in appendix F. The mean value over the entire population (87 electrodes) is 369k $\Omega$  and the sample standard deviation is 213k $\Omega$ . Three outliers of >1 M $\Omega$  are present in this population. After excluding the three outliers the total mean was 331k $\Omega$  with a SD of 71k $\Omega$ .

### 4.3 In-vivo test

Finally, an in-vivo test was done by implanting the probes into a rat's brain by lowering the hyperdrive screws. The hyperdrive contained 7 probes and 2 tetrodes. The tetrodes were implanted for validating the measured signals of the probes. The surgical procedure is briefly explained.

#### 4.3.1 Surgical procedure

The rat was anesthetized with 5% isoflurane in an induction chamber. The scalp was shaved, and the rat's head was secured in a stereotaxic manipulator<sup>36</sup>. During the entire surgical procedure anaesthesia was maintained by a continuous flow of 0.5-2.0% isoflurane. The respiration and heart rate were monitored for determining the level of anaesthesia and the concentration of isoflurane was adapted when necessary. The body temperature was measured by a rectal probe and maintained by an electrical heating pad. The skull was exposed after disinfecting the scalp with iodine and IPA. Eight bone screws<sup>37</sup> were inserted in the skull. The ground for the electrophysiological recordings was attached to one of the bone screws. A circular craniotomy of  $\varnothing$ 4 mm was made 4 mm posterior to Bregma and 2.5 mm right from the sagittal suture, hereafter the dura mater was removed. Silicon grease and mineral oil were inserted into the craniotomy to protect the exit tip cannulae from fluidic intrusion. The hyperdrive exit tip was lowered half-way the craniotomy and the hyperdrive was fixed

<sup>36</sup> Stoelting Co., Wood Dale, Illinois, United States

<sup>37</sup> Fine science tools, Heidelberg, Germany

by light-curable dental cement<sup>38</sup> to the skull attachment flanges and bone screws. The skin was sutured and the probes were 1.5 mm lowered into the brain.

In a few days the probes were gradually lowered to the pyramidal cell layer of the hippocampus CA1 region. The insertion depth is validated by reviewing the electrophysiological signals. The pyramidal cell layer is identified by a growing sharp-wave ripple activity and exhibited firing patterns [64].



*Figure 41: Freely behaving animal one day after the implantation.*

At the time of writing, the hyperdrive has been implanted four weeks and is still attached properly. Electrophysiological signals from the pyramidal cell layer were obtained 1 week after surgery.

---

<sup>38</sup> SDI, Bayswater, Australia

### 4.3.2 Recorded data

A section of the recorded data from the 2x8 probe is given in figure 42. The sampling frequency of the data acquisition system<sup>39</sup> was 32 kHz.

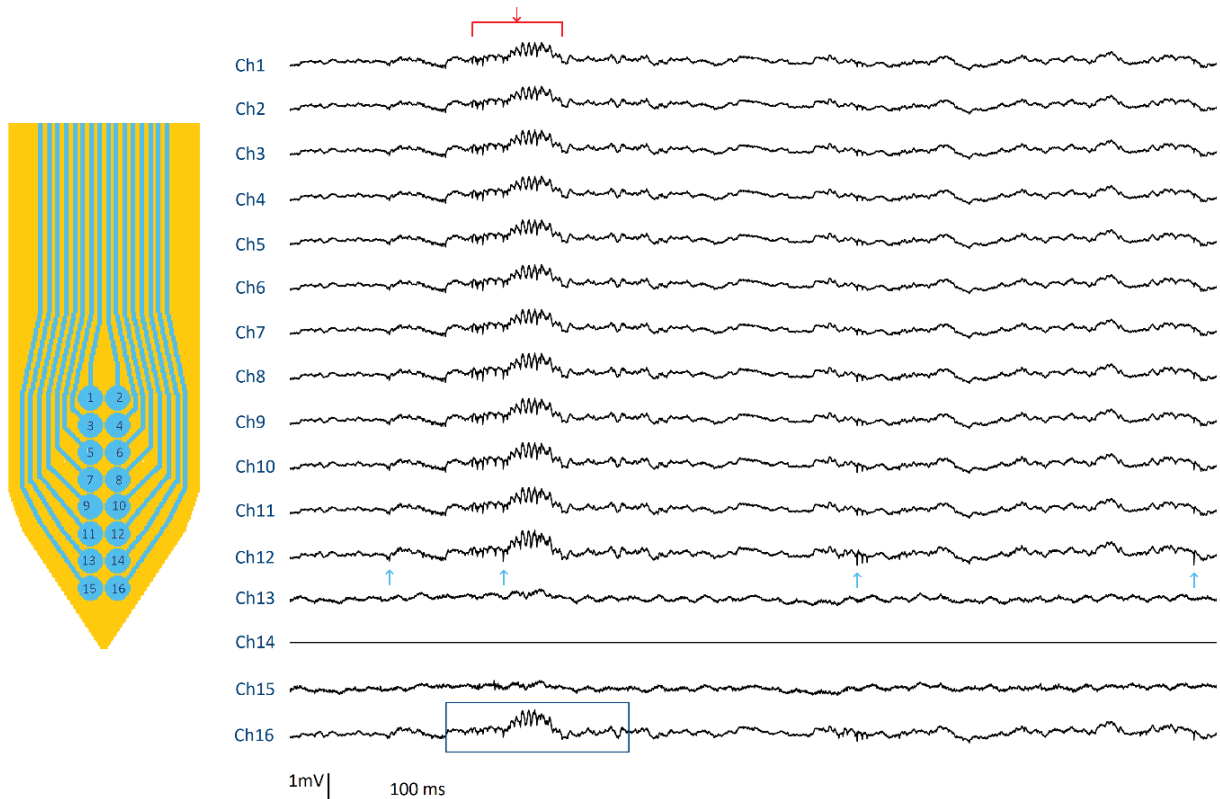


Figure 42: Hippocampal sharp-wave-ripples recorded by a 2x8 probe. The sharp-wave-ripple (red arrow) and high frequency spikes (blue arrows) indicates that the probe is located within the pyramidal cell layer of the hippocampus.

The channels Ch13, Ch14 and Ch15 correspond to the high impedance values given in table 4.

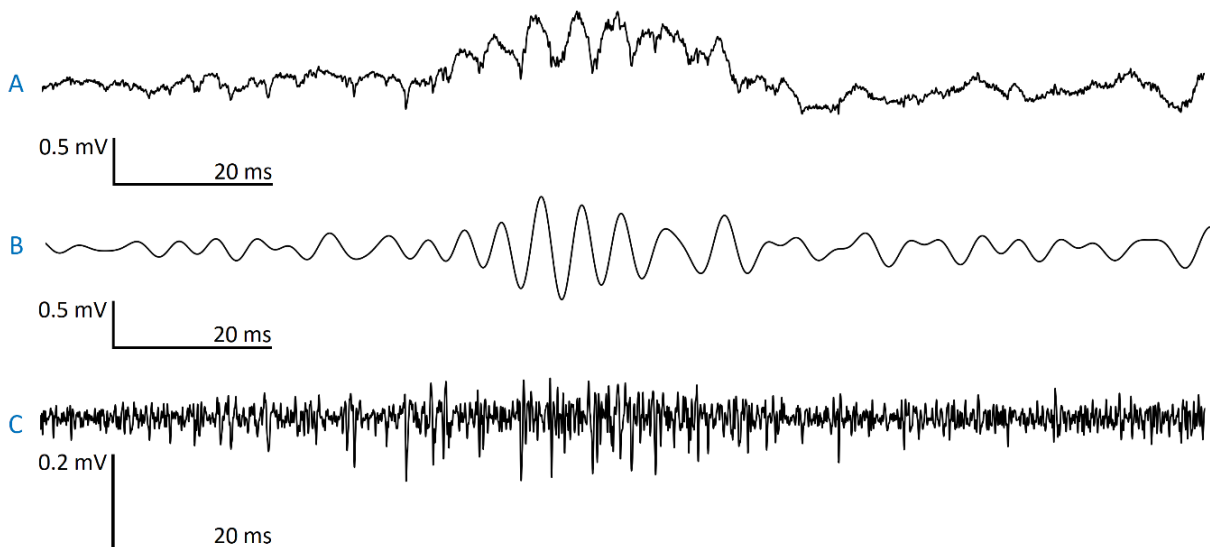


Figure 43: Zoomed section of the sharp-wave-ripple of channel 16. A) Raw data of channel 16. B) The raw data is band-pass filtered (100-230Hz) data showing the ripples. C) The raw data is high-pass filtered (>500 Hz) showing the neuronal spikes.

<sup>39</sup> Digital Lynx 4SX, Neuralynx, Bozeman, Montana, United States

The sharp-wave-ripple of Ch16 is magnified in figure 43A. A Kaiser bandpass filter between 100-230 Hz is applied to remove the high-frequency content revealing the ripples, see figure 43B. The low-frequency content was removed with the same filter by setting the filter band to 500-6000Hz revealing the spikes, see figure 43C.

To separate the different neurons semi-automatic spike sorting<sup>40</sup> was performed. Smart clustering and a greedy template matching approach was applied to sort the spikes. Even when two neurons had overlapping waveforms the spikes sorting algorithm could disentangle the waveforms. This is necessary because the electrode configurations are dense. The waveforms of the separated neurons are shown in figure 44. The channels are not corresponding to the previous probe channels.

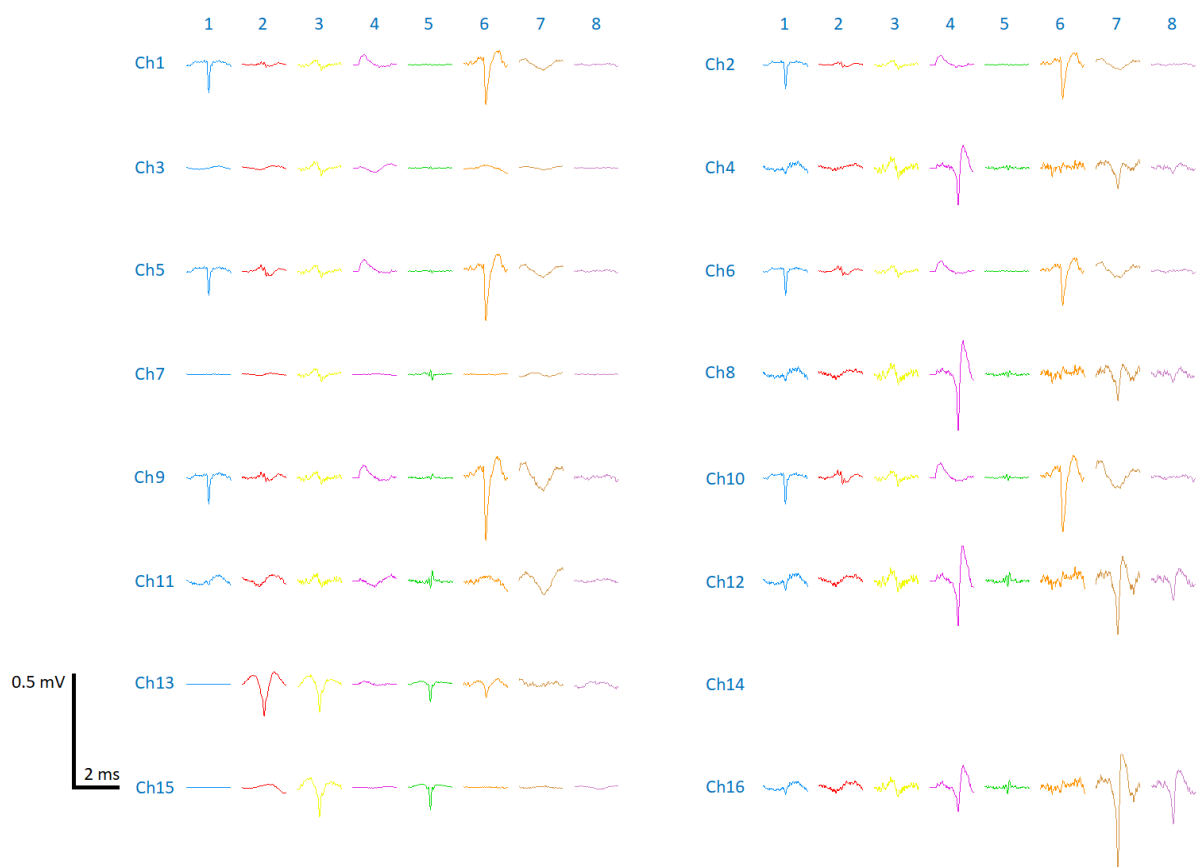


Figure 44: Eight isolated units recorded by a 2x8 probe.

<sup>40</sup> SpyKING CIRCUS

## 4.4 Discussion

In this study, electrophysiological signals obtained from a freely behaving animal were demonstrated. This shows the successful integration of the hyperdrive and flexible polyimide probes. Sharp-wave-ripples from the pyramidal cell layer were obtained with a 2x8 probe. A band-pass filter was applied revealing the hippocampal ripples and a high-pass filter was applied showing the spiking activity.

Three validation tests were performed: 1) an insertion test, 2) an impedance test, and 3) an *in-vivo* test. The insertion validation reveals that the probes penetrate 0.6% agarose gel till full depth but bend off track after three-fourth insertion. The current target area was the hippocampal CA1 pyramidal cell layer at approximately 2.5 mm, and bending is not an issue. Although if deeper brain areas are targeted or larger animals are used for electrophysiological recordings the probe should not bend off track. This problem can be solved by thickening the probe and hereby increasing the stiffness. Thickening can be implemented in a clever way by adding more electrodes in a stacked layer. Herewith the stiffness is increased and more single-units can be recorded. Literature describes several mechanisms to insert flexible probes into the brain tissue with the help of a retractable tool. For example lowering the probe through a needle. In this way a lot of tissue damage will occur. Another frequently applied method is coating the probe with a bioresorbable material, making the probe stiffer during insertion and no extra tool is needed. Unfortunately this method cannot be applied here as the probes are lowered gradually over time and retraction is sometimes necessary. After the insertion test the electrode impedance was validated.

The electrical impedance of the individual electrodes was validated with the impedance tester NanoZ. NanoZ simplifies the test as all electrodes on the probe can be tested at once. The initial impedance values were too high for performing electrophysiological experiments, hence a gold plating step was applied. By gold plating the impedance values dropped significantly to a mean value of 293k $\Omega$  with a sample standard deviation of 3.45 k $\Omega$ . However after testing the impedances again it was noticed that the values raised again. The adherence of platinum and plated gold seems not so good. Therefore plating with PEDOT<sup>41</sup> or platinum black<sup>42</sup> should be considered. To obtain instantly low impedance values the electrodes should be deposited with iridium oxide during the production, making gold plating not needed. After lowering the impedance values of the electrodes the hyperdrive was implanted. Sharp-wave-ripple activity near the hippocampal CA1 pyramidal cell layer was recorded and the spiking activity could be clustered. In total 8 neurons were registered with a 2x8 flexible polyimide probe lowered by the new hyperdrive. This is the proof of concept for the novel brain implant.

---

<sup>41</sup> Poly(3,4-ethylenedioxythiophene)

<sup>42</sup> Neuralynx, Bozeman, Montana, United States

## Chapter 5: Discussion

A novel hyperdrive with 16 individually movable microdrives for electrophysiological experiments is presented. Each microdrive carries a flexible polyimide probe with 16 recording electrodes, adding up to a total of 256 recording sites. Each probe is guided through a polyimide tube and 3D-printed titanium exit tip before penetrating the rat's brain. Electrophysiological recordings were obtained from the hippocampal pyramidal cell layer, demonstrating that the brain implant functions properly.

Four different flexible polyimide probes with 16 recording electrodes each were produced by micromachining technology. The 3x5+1 and 4x4 designs are more applicable for recording from dense target regions like the hippocampal pyramidal cell layer, while the 1x16 and 2x8 designs are more appropriate for targeting thicker structures, across several layers, like the cortex. After reaching the target, the thin and flexible polyimide probes move in unison with the brain and therefore create less damage than rigid silicon probes.

The hyperdrive dimensions and weight are significantly reduced in comparison to the previous design used at NERF. The assembly time for the new hyperdrive is approximately 1 day which is a considerable reduction compared to the previous design where the assembly lasted approximately two weeks. The electrical components are well protected within the hyperdrive so the neuroscientist is unable to accidentally hit a wire electrode when manipulating a microdrive.

Along the probe development several problems were encountered. The lift-off process has a substantial amount of parameters to be controlled. Some optimizations were implemented, e.g. the large amount of developer for the photoresist can be considered as constant. The interconnection lines from the electrodes to connector pads should be fanned out to increase the spacing between the lines and the probe length should be reduced to decrease the number of line failures. A layer of iridium oxide could be introduced on the electrodes because it does not exhibit corrosion and has a noteworthy surface roughness which increases the surface area and thus lowers the impedance of the electrodes [24]. If the electrode impedance is low enough ( $<300\text{ k}\Omega$ ), the electrode diameter could be reduced and herewith decreasing the probe width. In this work single layer polyimide probes were used, here the electrodes are all in the same plane. Multilayer probes, i.e. stacking the interconnection lines, will improve the spike sorting as the electrodes differ in three dimensions. Additionally, multilayer probes reduce the probe width for an equal number of electrodes [24].

The insertion test showed that the probes could penetrate agarose gel, although it bended of track after three-fourth insertion. From this it is concluded that stiffer probes are necessary when targeting deeper brain regions. Several techniques were discussed to target deep brain structures, whereof the most desirable solution is to improve the probe itself. When using the same materials, stiffening can be done in a clever way by stacking the metallization layers. Hereby the probe width is reduced and thickness is increased or the thickness is increased and more electrodes can be add. Although, the flexibility to move in unison with the brain decreases, making this a trade-off. Ideally a microfluidic channel, with e.g. a magnetorheological fluid, can be implemented into the probe shank, so that the stiffness can be increased during insertion and decreased after implantation.

The electrode impedances were sufficiently lowered by gold plating with a mean of 331k $\Omega$  and sample SD of 71k $\Omega$  after exclusion of the outliers. In the future it is preferred to produce electrodes with low impedance values initially to make plating unnecessary.

The probes were implanted into a rat's brain by gradually lowering shuttles within the hyperdrive. Sharp-wave-ripple activity was recorded and the spiking activity could be clustered. Single unit activity was recorded from 8 isolated neurons with a 2x8 flexible polyimide probe lowered by the new hyperdrive design. This is the most significant proof of the novel brain implant and shows that the system can be extended to target more distributed brain regions in freely behaving animals.

Future suggestions for the brain implant are the implementation of: motors to drive the probes downwards, wireless connectors or signal processing chips to improve the invasive electrophysiological recordings. Those technical advances will open new doors for complex behavioural experiments, like implementing a 3D-maze, and are very valuable for advancing the understanding of brain functioning. Acquiring more knowledge about proper brain functioning will evolve the treatments for various neurological disorders and tremendously impact the entire healthcare sector. The preceding is only realized by performing electrophysiological experiments and by implementing sophisticated tools like the brain implant presented in this thesis.

## References

- [1] E. R. Kandel, "In search of memory: the emergence of a new science of mind," ed. New York: W.W. Norton & Company, Inc., 2006.
- [2] M. Eckert and M. Tatsonu, *Overview of Neural Activity in the Awake and Sleeping Hippocampus* (Analysis and modelling of coordinated multi-neural activity). Lethbridge, Alberta, Canada: Springer, 2015.
- [3] F. Amthor, "Neuroscience for dummies", ed. Hoboken, New Jersey: John Wiley & Sons, 2016.
- [4] A. A. Fenton, K. J. Jeffery, and J. G. Donnett, "Electrophysiological recording techniques: Neural Recording Using Digital Telemetry", ed: Springer, 2011.
- [5] H. W. Steenland and B. L. McNaughton, *Techniques for Large-Scale Multiunit Recording* (Analysis and Modeling of Coordinated Multi-Neuronal Activity). Springer, 2015, pp. 3-39.
- [6] R. Venkateswaran, C. Boldt, B. Ziaie, A. G. Erdman, and A. D. Redish, "A motorized microdrive for recording of neural ensembles in awake behaving rats", *Journal of Biomechanical Engineering-Transactions of the Asme*, vol. 127, no. 6, pp. 1035-1040, 2005.
- [7] B. L. McNaughton, "Implantable multi-electrode microdrive array", Patent US 5928143, 1999.
- [8] F. Kloosterman *et al.*, "Micro-drive array for chronic in vivo recording: drive fabrication", *J Vis Exp*, no. 26, 2009.
- [9] L. R. Squire, "Memory and the Hippocampus: A Synthesis From Findings With Rats, Monkeys, and Humans", vol. 99, ed: Physiological Review, 1992, pp. 195-132.
- [10] J. O'Keefe and L. Nadel, "The hippocampus as a cognitive map", ed. Oxford: Clarendon Press, 1978.
- [11] M. Schünke, E. Schulte, U. Schumacher, M. Voll, and K. Wesker, "Prometheus Hoofd, hals en neuroanatomie," ed. Houten: Bohn Stafleu van Loghum, 2010.
- [12] J. M. Bekkers, "Pyramidal neurons," vol. 21, ed: Cell Press, Current Biology, 2011.
- [13] N. Spruston, "Pyramidal neurons: dendritic structure and synaptic integration," vol. 9, ed: Nature Neuroscience, 2008.
- [14] Atlas3D Neural Systems and Graphics Computing Laboratory, Atlas3D, 2017.
- [15] G. Paxinos and C. Watson, "The rat brain atlas in stereotaxic coordinates 6th edition", ed: Elsevier, 2007.
- [16] F. P. Battaglia *et al.*, "The Lantern: an ultra-light micro-drive for multi-tetrode recordings in mice and other small animals", *J Neurosci Methods*, vol. 178, no. 2, pp. 291-300, 2009.
- [17] B. L. McNaughton, J. O'Keefe, and C. A. Barnes, "The stereotrode: a new technique for simultaneous isolation of several single units in the central nervous system from multiple unit records", vol. 8, ed: Journal of Neuroscience Methods, 1983, pp. 391-397.
- [18] M. Vandecasteele *et al.*, "Large-scale recording of neurons by movable silicon probes in behaving rodents", *J Vis Exp*, no. 61, p. e3568, 2012.
- [19] D. P. Nguyen *et al.*, "Micro-drive array for chronic in vivo recording: tetrode assembly", *J Vis Exp*, no. 26, 2009.
- [20] J. H. Chung, F. Sharif, D. J. Jung, S. Kim, and S. Royer, "Micro-drive and headgear for chronic implant and recovery of optoelectronic probes", *Scientific Reports*, vol. 7, 2017, Art. no. 2773.
- [21] M. Jeon *et al.*, "Partially flexible MEMS neural probe composed of polyimide and sucrose gel for reducing brain damage during and after implantation", vol. 24, ed: Journal of Micromechanics and Microengineering, 2014.
- [22] R. A. Weale, "A new micro-electrode for Electrophysiological work", ed: Nature, 1951, pp. 529-530.
- [23] F. Windels, "Using Place Cells in Goal-Directed Behaviour: Rodent Electrophysiology", ed. Brisbane: The University of Queensland.
- [24] K. C. Cheung, P. Renaud, H. Tanila, and K. Djupsund, "Flexible polyimide microelectrode array for in vivo recordings and current source density analysis", *Biosensors and Bioelectronics*, vol. 22, no. 8, pp. 1783-1790, 2007.

- [25] S. H. Felix *et al.*, "Insertion of Flexible Neural Probes Using Rigid Stiffeners Attached with Biodissolvable Adhesive", vol. 79, ed: Journal of visualized experiments, 2013.
- [26] D. Egert, R. L. Peterson, and K. Najafi, "Parylene microprobes with engineered stiffness and shape for improved insertion", ed: Actuators and microsystems conference (Transducers), 2011.
- [27] K. Lee, A. Singh, J. He, S. Massia, B. Kima, and G. Raupp, "Polyimide based neural implants with stiffness improvement", vol. 102, ed: Sensors and Actuators, 2004, pp. 67-72.
- [28] L. Luan *et al.*, "Ultraflexible nanoelectronic probes form reliable, glial scar-free neural integration", vol. 3, ed: Science Advances, 2017.
- [29] J. J. Jun *et al.*, "Fully integrated silicon probes for high-density recording of neural activity", vol. 551, ed: Nature, 2017, pp. 232-236.
- [30] Mercanzini A. *et al.*, "Demonstration of cortical recording using novel flexible polymer neural probes", vol. 143, ed: Sensors and Actuators, 2008, pp. 90-96.
- [31] N. Maluf and K. Williams, *An introduction to microelectromechanical systems engineering*, Second ed. Norwood, Massachusetts, USA: Artech house inc., 2004.
- [32] P. Walker and W. H. Tarn, "Handbook of metal etchants", ed. Boca Raton, Florida: CRC Press, 1990.
- [33] K. M. Liecht, A. Shirani, R. G. Dillingham, F. J. Boerio, and S. M. Weaver, "Cohesive Zone Models of Polyimide/Aluminum Interphases", vol. 73:2-3, ed: The Journal of Adhesion, 2000, pp. 259-297.
- [34] S. Franssila, "Introduction to microfabrication", ed: John Wiley and Sons, 2010.
- [35] Nanofilm, Westlake Village, CA 91361, <http://www.nanofilm.com/>
- [36] MicroChem, "LOR Lift-off resists", ed. Newton, Massachusetts.
- [37] Rohm and Haas Electronic Materials, "Microposit S1800 G2 series photoresist for microlithography applications", ed: Philadelphia U.S.
- [38] M. Brunetti *et al.*, "Design and fabrication of ultralight weight, Adjustable multi-electrode probes for electrophysiological recordings in mice", *Journal of Visualized Experiments*, no. 91, 2014.
- [39] S. Yang *et al.*, "Feedback controlled piezo-motor microdrive for accurate electrode positioning in chronic single unit recording in behaving mice", *J Neurosci Methods*, vol. 195, no. 2, pp. 117-27, 2011.
- [40] P. L. Lu *et al.*, "Microdrive with Two Independent Moveable Sets for Wide-Ranging, Multi-Site, Multi-Channel Brain Recordings," *Journal of Medical and Biological Engineering*, vol. 34, no. 4, pp. 341-346, 2014.
- [41] S. Park *et al.*, "The development of a PZT-based microdrive for neural signal recording," *Smart Materials and Structures*, vol. 17, no. 2, 2008.
- [42] J. W. Aldridge, A. Klein, and M. Bradshaw, "Hybrid multichannel printed circuit board microdrive", Patent US 08428680, 2013.
- [43] J. X. Zhang and R. M. Harper, "A new microdrive for extracellular recording of single neurons using fine wires", *Electroencephalogr Clin Neurophysiol*, vol. 57, no. 4, pp. 392-4, 1984.
- [44] A. Jovalekic *et al.*, "A lightweight feedback-controlled microdrive for chronic neural recordings", *J Neural Eng*, vol. 14, no. 2, p. 026006, 2017.
- [45] Neuralynx, "Halo-10/Halo-18 Microdrive User's Manual Microdrive used for manually driving tetrodes for electrophysiology recordings. Revised version 1.2", ed. Bozeman, 2017.
- [46] D. A. Henze, "Microdrive for modular microdrive assembly for positioning instrument in body of animal, has drive rod rotated in one direction, producing force at the complementary contact which urges carriage closer to surface of body", Patent WO2009032838-A1; US2010211081-A1.
- [47] F. Haiss, S. Butovas, and C. Schwarz, "A miniaturized chronic microelectrode drive for awake behaving head restrained mice and rats", *J Neurosci Methods*, vol. 187, no. 1, pp. 67-72, 2010.

- [48] D. B. Headley, M. V. DeLuca, D. Haufler, and D. Paré, "Incorporating 3D-printing technology in the design of head-caps and electrode drives for recording neurons in multiple brain regions", *J Neurophysiol*, vol. 113, no. 7, pp. 2721-32, 2015.
- [49] "Halo-10/Halo-18 Microdrive User's Manual Microdrive used for manually driving tetrodes for electrophysiology recordings. Revised version 1.2", ed. Bozeman, 2017.
- [50] M. S. Fee and A. Leonardo, "Miniature motorized microdrive and commutator system for chronic neural recording in small animals", *J Neurosci Methods*, vol. 112, no. 2, pp. 83-94, 2001.
- [51] J. Yamamoto and M. A. Wilson, "Large-scale chronically implantable precision motorized microdrive array for freely behaving animals", *J Neurophysiol*, vol. 100, no. 4, pp. 2430-40, 2008.
- [52] J. Yamamoto, *Next Generation Large-Scale Chronically Implantable Precision Motorized Microdrive Arrays for Freely Behaving Animals* (Advances in Cognitive Neurodynamics), 2011, pp. 67-72.
- [53] I. Szabó, A. Czurkó, J. Csicsvari, H. Hirase, X. Leinekugel, and G. Buzsáki, "The application of printed circuit board technology for fabrication of multi-channel micro-drives", *J Neurosci Methods*, vol. 105, no. 1, pp. 105-10, 2001.
- [54] T. M. Otchy and B. P. Ölveczky, "Design and assembly of an ultra-light motorized microdrive for chronic neural recordings in small animals", *J Vis Exp*, no. 69, 2012.
- [55] M. S. Jog *et al.*, "Tetrode technology: advances in implantable hardware, neuroimaging, and data analysis techniques", *Journal of Neuroscience Methods*, vol. 117, no. 2, pp. 141-152, 2002.
- [56] E. B. Contreras, S. Chekhov, J. Sun, J. Tarnowsky, B. L. McNaughton, and M. H. Mohajerani, "High-performance, inexpensive setup for simultaneous multisite recording of electrophysiological signals and mesoscale voltage imaging in the mouse cortex," vol. 5, ed: Neurophotonic, 2018.
- [57] H. D. Dobbins, P. Marvit, Y. D. Ji, and D. A. Depireux, "Chronically recording with a multi-electrode array device in the auditory cortex of an awake ferret," *Journal of Neuroscience Methods*, vol. 161, no. 1, pp. 101-111, 2007.
- [58] D. S. Freedman, J. B. Schroeder, G. I. Telian, Z. Y. Zhang, S. Sunil, and J. T. Ritt, "OptoZIF Drive: a 3D printed implant and assembly tool package for neural recording and optical stimulation in freely moving mice", *Journal of Neural Engineering*, vol. 13, no. 6, 2016.
- [59] F. Michon *et al.*, "Integration of silicon-based neural probes and micro-drive arrays for chronic recording of large populations of neurons in behaving animals", *J Neural Eng*, vol. 13, no. 4, p. 046018, 2016.
- [60] Neuralynx, "Harlan 28 Drive User Manual: Microdrive used for manually driving tetrodes for electrophysiology recordings," ed. Bozeman, 2013.
- [61] J. Voigts, J. H. Siegle, D. L. Pritchett, and C. I. Moore, "The flexDrive: an ultra-light implant for optical control and highly parallel chronic recording of neuronal ensembles in freely moving mice", *Front Syst Neurosci*, vol. 7, p. 8, 2013.
- [62] T. Sato, T. Suzuki, and K. Mabuchi, "A new multi-electrode array design for chronic neural recording, with independent and automatic hydraulic positioning", *J Neurosci Methods*, vol. 160, no. 1, pp. 45-51, 2007.
- [63] J. Muthuswamy, M. Okandan, T. Jain, and A. Gilletti, "Electrostatic microactuators for precise positioning of neural microelectrodes", *Ieee Transactions on Biomedical Engineering*, vol. 52, no. 10, pp. 1748-1755, 2005.
- [64] C. S. Lansink *et al.*, "A split microdrive for simultaneous multi-electrode recordings from two brain areas in awake small animals", *J Neurosci Methods*, vol. 162, no. 1-2, pp. 129-38, 2007.
- [65] R. C. deCharms, D. T. Blake, and M. M. Merzenich, "A multielectrode implant device for the cerebral cortex", *J Neurosci Methods*, vol. 93, no. 1, pp. 27-35, 1999.
- [66] K. A. Stengel and R. S. Olson, "Multi-electrode microdrive array," Patent US 07769421, 2010.
- [67] "Harlan 28 Drive User Manual: Microdrive used for manually driving tetrodes for electrophysiology recordings," ed. Bozeman, 2013.

- [68] Y. Jeantet and Y. H. Cho, "Design of a twin tetrode microdrive and headstage for hippocampal single unit recordings in behaving mice", *J Neurosci Methods*, vol. 129, no. 2, pp. 129-34, 2003.
- [69] Formlabs, 2018, Available: <https://formlabs.com/>
- [70] B. Redwood, F. Schöffner, and B. Garret, "The 3D printing handbook Technologies, design and applications," ed. Amsterdam: 3D Hubs, 2017.
- [71] J. F. Ready, "LIA handbook of laser materials processing," ed. Orlando: Laser Institute of America, 2001.
- [72] C. L. Caristan, "Laser cutting guide for manufacturing," ed. Dearborn, Michigan: Society of manufacturing Engineers, 2004.
- [73] Elektriska Svetsnings-Aktiebolaget (ESAB), 2018, *How does laser cutting work?* Available: [www.esabna.com](http://www.esabna.com)
- [74] M. A. Erismis, H. P. Neves, P. D. Moor, R. Puers, and C. V. Hoof, "A water-tight packaging of MEMS electrostatic actuatorsfor biomedical applications," vol. 16, ed: Microsystem Technologies, 2010, pp. 2109–2113.

## Annexes

### A: Method of the literature study

In the literature study several databases were searched: PubMed, ScienceDirect, Scopus. The search engine Web of Science was used to simplify the search. A search through all databases of Web of Science was also performed, including Inspec<sup>®43</sup>. The following terms were applied in those databases: Kloosterman F, micro-drive, microdrive, microdrive array, micro-drive array, microdrive AND rodents, microdrive AND rats, micro-drive AND rodents, micro-drive AND rats. The obtained articles were imported into EndNote™ basic for plain arrangement.

Inclusion criteria: microdrive, microdrive array, motorized microdrive, rodents, rats, mice, neurology, hippocampus, cortex, place cells, pyramid cells, replay, awake animals, freely behaving. The article needs to describe a device for lowering multiple recording electrodes, e.g. probes, tetrodes, stereotrodes, into the brain. The recording device should be independently adjustable during or in between experiments.

Exclusion criteria: papers that described a brain recording device applicable for other subjects than rodents, e.g. monkeys, non-human primates, frogs, fishes, zebra finches, rabbits, cats. Papers that described a fixed setup, e.g. a stereotaxic manipulator, instead of a hyperdrive for inserting the recording electrodes. Papers that were not written in English, Dutch or German.

### Results

The entire filtering procedure is depicted in figure 45. A total of 1733 references remained by searching the above given databanks with the applied search terms and automatically filtering for duplicates.

Subsequently, the remained duplicates were manually discarded in parallel with a filtering for relevant titles, 217 articles remained. Titles that did not yield an engineering content related to microdrive design for brain recordings were excluded.

Where after the articles were filtered based on their abstract content. Articles were discarded if only the abstracts of articles were available or if the content of the abstract was not matching the inclusion and exclusion criteria. Articles which described another type of brain implant were excluded from the research, e.g. a brain recording telemetry system for zebra finches.

---

<sup>43</sup> Inspec<sup>®</sup> is a database of scientific and technical literature, published by the Institution of Engineering and Technology (IET)

After applying the inclusion and exclusion criteria a total of 63 articles remained. Those articles were thoroughly read, whereof 39 papers were used in the master's thesis.

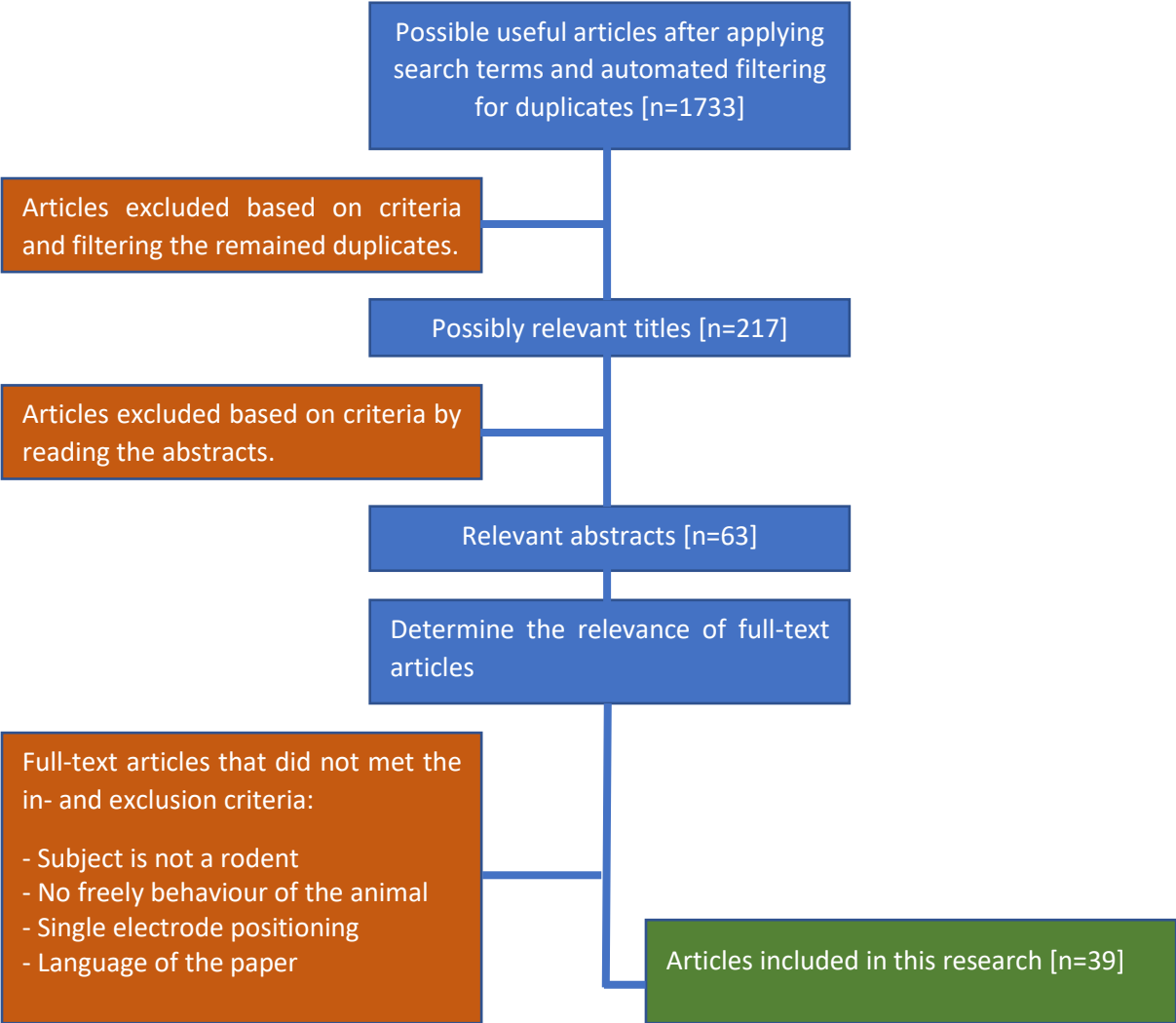


Figure 45: Filtering procedure for the literature study.

B: Results and methods for the individual wafers

Wafer #	Diced parts	Lift-off resist & spinning speed [rpm]	Photolithography dose [mJ/cm]	Development time [min.]	Substrate surface	Metal & deposition method	Result
1	A	LOR3A 1500 rpm	23	1:45 & shaking	Silicon	Al evaporation	Paths lift-off
	B		23	2:00 & shaking	Silicon		Paths lift-off
	C		23	2:15 & shaking	Silicon		Paths lift-off
	D		23	2:30 & shaking	Silicon		Paths lift-off
2	A	LOR10B 3500 rpm	23	1:45 & shaking	Silicon	Al evaporation	Paths lift-off
	B		23	2:00 & shaking	Silicon		Paths remained
	C		23	2:15 & shaking	Silicon		Paths remained
	D		23	2:25 & shaking	Silicon		Paths remained
3	A	LOR3A 1500 rpm	23	2:45 & shaking	Silicon	Al sputtering 2x 15min. at 100W with 10 min. pause in between (35nm/min.)	Paths lift-off
	B		23	3:00 & shaking	Silicon		Paths lift-off
	C		23	3:15 & shaking	Silicon		Paths lift-off
	D		23	3:30 & shaking	Silicon		Paths lift-off
	E		23	3:55 & shaking	Silicon		Paths lift-off
4	A	LOR10B 3500 rpm	23	2:00 & shaking	Silicon	Al sputtering 2x 15min. at 100W with 10 min. pause in between (35nm/min.)	Paths lift-off
	B		23	2:15 & shaking	Silicon		Paths lift-off
	C		23	2:25 & shaking	Silicon		Uncertain
5	A	LOR3A 1500 rpm	26	4:30 & shaking	Silicon		Paths lift-off
	B		26	5:00 & shaking	Silicon		Paths lift-off

	C		26	14:40 & shaking	Silicon	Al sputtering 2x 15min. at 100W with 10 min. pause in between (35nm/min.)	Paths lift-off
6	A	LOR10B 3500rpm	26	2:25 & shaking	Silicon	Al sputtering 2x 15min. at 100W with 10 min. pause in between (35nm/min.)	Paths lift-off
	B		26	2:45 & shaking	Silicon		Uncertain
	C		26	3:00 & shaking	Silicon		Too long developed
7		LOR10B 3500 rpm	23	2:30 & shaking	Polyimide	300 nm Pt-IrOx sputtering	Particles between lines
8		LOR10B 3500 rpm	23	2:30 & shaking	Polyimide	300nm Pt-IrOx sputtering	Particles between lines
9		LOR10B 3500 rpm	23	2:30 & shaking	Polyimide	300nm Pt-IrOx sputtering	Particles between lines
10		LOR10B 3500 rpm	23	2:30 & shaking	Polyimide	300nm Pt-IrOx sputtering	Particles between lines
11		LOR10B 3500 rpm	23	1:30 & shaking	Polyimide	300nm Pt-IrOx sputtering	Particles between lines
12		LOR10B 3500 rpm	23	1:30 & shaking	Polyimide	300nm Pt-IrOx sputtering	Particles between lines
13		LOR10B 3500 rpm	23	1:30 & shaking	Polyimide	300nm Pt-IrOx sputtering	Particles between lines

14	LOR10B 3500 rpm	23	1:30 & shaking	Polyimide	300nm Pt-IrOx sputtering	Particles between lines
15	LOR10B 3500 rpm	23	2:25 shaking 15 sec. at begin and end	Polyimide	300nm Pt-IrOx sputtering	Paths lift-off
16	LOR10B 3500 rpm	23	2:35 shaking 15 sec. at begin and end	Polyimide	300nm Pt-IrOx sputtering	Paths lift-off
17	LOR10B 3500 rpm	23	2:25 shaking 15 sec. at begin and end	Polyimide	300nm Pt-IrOx sputtering	Paths lift-off
18	LOR10B 3500 rpm	23	2:25 shaking 15 sec. at begin and end	Polyimide	300nm Pt-IrOx sputtering	Particles between lines
19	LOR10B 3500 rpm	23	2:25 shaking 15 sec. at begin and end	Polyimide	300nm Pt-IrOx sputtering	Paths lift-off
20	LOR10B 3500 rpm	23	2:25 shaking 15 sec. at begin and end	Polyimide	N.A.	Photoresist too long developed
21	LOR10B 3500 rpm	23	2:25 shaking 15 sec. at begin and end	Polyimide	300nm Pt-IrOx sputtering	Particles between lines
22	LOR10B 3500 rpm	23	2:25 shaking 15 sec. at begin and end	Polyimide	N.A.	Photoresist too long developed
23	LOR10B 9000 rpm	23	2:15 shaking 15 sec. at begin and end	Polyimide	300nm Pt-IrOx sputtering	Some paths gone and particles between lines

24	LOR3A 1800 rpm	23	4:00 shaking 15 sec. at begin and end	Polyimide	300nm Pt-IrOx sputtering	Some paths gone and particles between lines
25	LOR10B 3500 rpm	23	2:35 shaking 15 sec. at begin and end	Polyimide	20nm Pt sputter + 80 nm Pt evaporation	Some disconnected lines but acceptable
26	LOR10B 3500 rpm	23	2:25 shaking 15 sec. at begin and end	Polyimide	20nm Pt sputter + 80 nm Pt evaporation	Some disconnected lines but acceptable
27	LOR10B 3500 rpm	23	2:25 shaking 15 sec. at begin and end	Polyimide	20nm Pt sputter + 80 nm Pt evaporation	Not processed
28	LOR10B 9000 rpm	23	2:45 shaking 15 sec. at begin and end	Polyimide	20nm Pt sputter + 80 nm Pt evaporation	Not processed

C: Individual part weights of the hyperdrive

<b>Individual parts</b>	<b>[gr]</b>
Main body	8,255
Permanent cap	2,178
Removable cap	2,85
Cone & Skull attachment	2,235
Custom screws (16x)	1,66
Stainless steel shuttles (16x)	0,834
Ring magnets (4x)	1,486
EIB (approximately)	3,5
Exit tip	0,25
Washers (4x)	0,3934
3mm M1.2 screws (12x)	0,427
Dental cement approximation	0,192
Polyimide 141-0005	0,0832
Polyimide 141-0003	0,008
Gold socket (3x)	0,057
Gold pins (2x)	0,02
Threaded inserts M1.2 (12x)	0,425
Probes (16x)	N.A.
Grounding wire	0,0018
<b>Total weight [gr]</b>	<b>24,8554</b>

## D: Channel mapping

NanoZ Nlx-EIB-36	Omnetics 44pin EIB-36	AtlasNeuro Omnetics	AtlasNeuro EIB ZIF7	2x8 Probe channel
1	A1	19	p10	15
2	A2	18	p11	11
3	A3	17	p12	7
4	A4	16	p13	3
5	A5	15	p14	2
6	A6	14	p15	6
7	A7	13	p16	10
8	A8	12	p17	14
9	A9	11	p4	4
10	A10	10	p3	8
11	A11	9	p2	12
12	A12	8	p1	16
13	A13	7	p5	1
14	A14	6	p6	5
15	A15	5	p7	9
16	A16	4	p8	13

Probe channel mapping according to figure 42.

## E: Probe configuration within the hyperdrive

Microdrive number	1	2	3	4	5	6	7	8	9	10	11	12	13	14	15	16
ZIF number on EIB	7		T4		T1	5				4	3		2	1		8
Probe configuration	2x8		tet.		tet.	2x8				1x16	2x8		2x8	3x5		3x5
Working electrodes	13		4		4	12				4	11		10	11		13

## F: Impedance values of probes within hyperdrive

Probe 2x8 Ch7 of ZIF		Probe 2x8 Ch5 of ZIF		Probe 1x16 Ch 4 of ZIF		Probe 2x8 Ch3 of ZIF		Probe 2x8 Ch2 of ZIF		Probe 3x5 Ch1 of ZIF		Probe 3x5 Ch8 of ZIF	
EIB-36 #	MΩ	EIB-36 #	MΩ	EIB-36 #	MΩ	EIB-36 #	MΩ	EIB-36 #	MΩ	EIB-36 #	MΩ	EIB-36 #	MΩ
2	0,296	18	0,333	18	0,295	2	0,299	17	0,29	1	0,313	17	0,356
3	0,298	19	0,298	19	0,309	3	0,284	18	0,294	2	0,294	18	0,329
4	0,291	20	0,294	20	0,36	4	0,283	19	0,327	3	0,29	19	0,359
5	0,289	21	0,367	21	0,325	5	0,286	20	0,295	4	0,293	20	0,284
6	0,292	24	0,408	22	0,382	6	0,222	22	0,293	7	0,296	21	0,319
7	0,291	25	0,321	23	0,388	7	0,322	23	0,295	8	0,287	22	0,746
9	0,294	26	0,293	25	0,489	8	0,295	26	0,296	11	0,292	23	0,293
10	0,289	27	0,313	26	0,329	9	0,285	27	0,318	12	0,364	24	1,299
11	0,298	28	1,516	27	0,365	10	0,433	28	0,364	13	1,453	26	0,309
12	0,294	29	0,34	28	0,341	11	0,334	29	0,47	14	0,297	27	0,468
13	0,294	31	0,306	29	0,362	14	0,294	30	0,327	16	0,296	29	0,379
14	0,287	32	0,301	30	0,345	15	0,292	31	0,39			31	0,508
15	0,295			31	0,293	16	0,515						
				32	0,395								

<b>Working channels</b>	13	12	14	13	12	11	12
<b>% of 16</b>	81%	75%	88%	81%	75%	69%	75%
<b>Mean [MΩ]</b>	0,293	0,424	0,356	0,319	0,330	0,407	0,471
<b>Sample SD [MΩ]</b>	0,003	0,346	0,050	0,075	0,054	0,348	0,291
<b>Mean w/o outliers [MΩ]</b>		0,325				0,302	0,395
<b>Mean w/o outliers [MΩ]</b>		0,036				0,023	0,136
<b>Total mean [MΩ]</b>	0,369						
<b>Total SD [MΩ]</b>	0,213						
<b>Total mean w/o outliers [MΩ]</b>	0,331						
<b>Total SD w/o outliers [MΩ]</b>	0,071						

The total mean and sample standard deviation are calculated over the entire population. An outlier is considered as a value above 1MΩ.